Atmospheric Research 310 (2024) 107616

Contents lists available at ScienceDirect

Atmospheric Research

journal homepage: www.elsevier.com/locate/atmosres

A long-term Doppler wind LiDAR study of heavy pollution episodes in western Yangtze River Delta region, China

Mengya Wang [a], Tianwen Wei [a,*], Simone Lolli [c], Kenan Wu [b], Yuan Wang [a], Hainan Hu [a], Jinlong Yuan [a], Dawei Tang [b], Haiyun Xia [a,b,*]

[a] Collaborative Innovation Centre on Forecast and Evaluation of Meteorological Disasters, China Meteorological Administration Aerosol-Cloud and Precipitation Key Laboratory, School of Atmospheric Physics, Nanjing University of Information Science & Technology, Nanjing, China

[b] School of Earth and Space Science, University of Science and Technology of China, Hefei 230026, China

[c] CNR-IMAA, Contrada S. Loja snc, Tito Scalo, PZ 85050, Italy

ARTICLE INFO

Keywords:
Doppler wind LiDAR
Aerosol backscatter coefficient
Wind profile
Heavy pollution episodes

ABSTRACT

Previous studies are primarily based on surface air pollution for a single event, leaving research on the temporal characteristics of aerosols and wind fields in the atmospheric boundary layer (ABL) and their associations unclear due to a lack of long-term vertical profile data. This study was the first to conduct long-term Doppler wind LiDAR measurements from Sep. 2019 to Aug. 2022 in Hefei in western Yangtze River Delta (YRD) region, China. The spatiotemporal characteristics of retrieved aerosol backscatter coefficient (β) and wind profiles were analyzed from the perspective of long-term statistics and typical heavy pollution episodes (HPEs). The seasonal profile of β showed a peak in the near-surface layer meanwhile the overall β profile (<0.5 km) was the highest in winter but lowest in summer. Combined with ground-based meteorological and air quality observations, 12 HPEs were identified and classified into dust-related events and fog-haze episodes. The results showed a consistency between hourly variations in PM_{10} (particulate matter smaller than 10 μm) concentration and β retrieved at 300 m during a high PM_{10} concentration (>150 μg/m^3) period. Different roles of horizontal wind at different altitudes and its associated time delay effect on surface PM_{10} pollution were evaluated based on correlation coefficients (Φ) and air pollution diffusion conditions. Significant positive Φ values were noticed below 0.5 km during the entire dust-related EP4 and EP6, indicating that the higher wind speeds could exacerbate PM_{10} pollution. In contrast, large negative Φ values meant the removal of PM_{10} pollutants by strong winds below 0.8 km during 24 h after peak in EP3. Combining with backward trajectory analysis and meteorological condition, notable transboundary pollution with positive contributions from upper winds (>1.5 km) was discovered in dust-related EP1, EP4, EP7, EP9, and EP10. Time delay effect (1-h/2-h lag) of upper winds (>0.8 km) on surface PM_{10} pollution was explored in EP5, EP6, EP7, EP8, and EP9. In spring dust-related HPEs, surface PM_{10} pollution was mostly contributed by long-range transport of aerosol particles at higher altitudes (>1.5 km) from the northwest direction, driven by the Mongolian cyclone and the cold front system. Transboundary aerosols originated from the northern part of Anhui province and the YRD region in the middle altitudes (~0.5 km) was the main contributor to fog-haze HPEs. The findings demonstrated the ability of the real-time Doppler wind LiDAR system to monitor transboundary air pollution and provided a scientific reference for policy makers.

1. Introduction

Air pollution is one of the major environmental problems that arises from various natural and anthropogenic emissions and has become the world's greatest environmental risk to health (Cory-Slechta and Sobolewski, 2023; Huang et al., 2018). The World Health Organization reported that 21% of China's disease burden is related to environmental pollution (Xia et al., 2022). Air quality is closely related to the concentration of air pollutants suspended in the atmosphere. Although air quality in China has improved substantially as a result of strict air pollution control policies, severe particles-related events, especially dust storms, occur frequently in spring in recent years. Fine particulate

* Corresponding authors at: Collaborative Innovation Centre on Forecast and Evaluation of Meteorological Disasters, China Meteorological Administration Aerosol-Cloud and Precipitation Key Laboratory, School of Atmospheric Physics, Nanjing University of Information Science & Technology, Nanjing, China.

E-mail addresses: twwei@nuist.edu.cn (T. Wei), hsia@ustc.edu.cn (H. Xia).

https://doi.org/10.1016/j.atmosres.2024.107616
Received 26 March 2024; Received in revised form 22 May 2024; Accepted 1 August 2024
Available online 3 August 2024

matter ($PM_{2.5}$) is composed of primary and secondary aerosols, which have complicated interactions with ozone (Ojha et al., 2022). Previous studies have investigated the adverse impact of $PM_{2.5}$ on tropospheric ozone formation through changing atmospheric dynamics and photolysis rates (He et al., 2022; Qu et al., 2020; Xing et al., 2017; Zong et al., 2021). The challenge of joint regulation of both ozone and $PM_{2.5}$ highlights the importance of improving our knowledge of air quality based on comprehensive measurements. Therefore, it is crucial to fully understand the spatial, temporal, and vertical characteristics of aerosol distribution during the formation, accumulation, and dissipation of air pollution.

The structure of the atmospheric boundary layer (ABL) plays a critical role in the complex dynamics of air pollutants through various physical processes and chemical reactions (Li et al., 2017; Miao et al., 2023). Many studies have reported significant positive associations between a shallower ABL and an increase in $PM_{2.5}$ concentration (Dupont et al., 2016; Miao et al., 2017). Past studies have investigated the influence of meteorological parameters at different heights on surface $PM_{2.5}$ pollution (Liu et al., 2022b; Luo et al., 2018). Zhang et al. (2020a) found a strong dependence of surface $PM_{2.5}$ pollution on vertical wind shear within the ABL based on radar wind profiler measurements in Beijing. Additionally, strong winds above the ABL also favored the transport of aerosols which could in turn deteriorate the surface $PM_{2.5}$ pollution through vertical mixing. Generally, weak synoptic winds with stable atmospheric stratification and shallow ABL conditions are conducive to accumulation of $PM_{2.5}$ pollution (He et al., 2022; Hung et al., 2020). However, the varying characteristics of vertical wind features in both lower and upper ABL and their associations with aerosol in the evolution of particle pollution process remain unclear. Hence, it leads to demand for synchronous observations of the vertical aerosol and wind profiles with high spatiotemporal resolution.

Long-term measurements of air pollutants are essential to better understand their temporal characteristics, particularly at different heights (Xiang et al., 2021; Yim and Huang, 2023). Passive remote sensing technology is a useful tool to fill the spatial disparity gap of air pollution measurements, whereas it lacks vertical information on objectives with high temporal resolution at different heights. Chemical transport models (CTMs) have been widely applied to assess spatiotemporal variations of air pollutants, but include uncertainties and biases in the model. Note that the performance of CTMs is highly dependent on the accuracy of model inputs. To complement the above shortages, Light Detection and Ranging (LiDAR) technology is employed to measure the vertical profiles of aerosol and winds. As an active remote sensing technology, LiDAR can provide range-resolved detection of atmospheric components (i.e., aerosol, ozone, water vapor, etc.) and meteorological parameters (i.e., wind, temperature, etc.) (Banah and Smalikho, 2013) with high spatiotemporal density, depending on different principles. Previous air quality studies using LiDAR measurements mainly focus on a typical pollution episode, while a long-term time series analysis is quite limited.

To date, studies of regional air pollution in China have mainly concentrated on several highly polluted regions accompanied by high urbanization and industrialization, such as the Beijing–Tianjin–Hebei (BTH), Yangtze River Delta (YRD) and Pearl River Delta (PRD) regions (Gu and Yim, 2016; Wang et al., 2015; Yang et al., 2021; Yang et al., 2020b; Liu et al., 2022a). However, relevant research in Anhui province in western YRD region is insufficient to warrant much more effort. Additionally, heavy aerosol pollution has been lastly reported to still occur frequently in this region in winter (Sulaymon et al., 2021; Yan et al., 2022). As the capital of Anhui province, Hefei has suffered severe air pollution problems due to the rapid growth of vehicles and population in recent years (Shi et al., 2018; Huang et al., 2020). Mao et al. (2019) reported that regional transport of aerosol sources from adjacent cities in the YRD region and remote regions could exacerbate air pollution in Hefei. Few studies conducted an experiment on vertical characteristics of air pollution during a pollution episode in Hefei based on LiDAR (Ren et al., 2022) or UAVs (Ren et al., 2022; Shen et al., 2022). It pinpoints the necessity to establish a real-time monitoring system to improve our knowledge about the mitigation of regional air pollution in Hefei. Therefore, it is necessary to investigate transboundary air pollution in Hefei in western YRD driven by different meteorological conditions.

This study conducted 3-year (Sep. 2019 ~ Aug. 2022) Doppler wind LiDAR measurements in Hefei in western YRD region. It aimed to systematically analyze the spatiotemporal characteristics of vertical aerosol backscatter coefficient (β) and wind profiles from the perspective of long-term statistics and typical heavy pollution episodes (HPEs). We identified several HPEs based on long-term LiDAR measurements, real-time monitoring data of surface air pollutants, ground-based meteorological observations, satellite data, and reanalysis data. We comprehensively analyze the characteristics of weather system, pollution process, vertical β, horizontal and vertical wind speed, and horizontal wind direction in and above the ABL. Furthermore, we assessed the association between β and wind profiles at different heights. The materials and methodology are described in section 2. Results and discussion are described in section 3 and section 4, respectively. Finally, the main findings are summarized in section 5.

2. Materials and methodology

2.1. Study region

Hefei is located to the west of the YRD region, China (31°52′ N, 117°17′ E) and in the middle of Anhui province (Fig. S1a). Hefei has three different types of landforms in the territory: hilly land, low mountains, and low-lying plains. Its terrain slopes from the northwest to southwest in main urban areas while its southwest part belongs to the remnants of Dabie Mountains. The averaged elevation ranges between 15 and 80 m. It has now become an emerging new first-tier city and experienced dramatic spatial expansion and economic growth in recent decades. As of 2019, Hefei covered a total area of 11,445.1 km^2 and had a resident population of 8,189,000 with an urbanization rate of 76.33% (Ye et al., 2021). The climate in Hefei is characterized by a subtropical monsoon type with four distinct seasons. The dense population and developed economy associated with substantial anthropogenic emissions have resulted in severe episodes of air pollution.

2.2. Doppler wind LiDAR system

In this study, a Doppler wind LiDAR system was applied to monitor the vertical profiles of aerosol backscatter coefficient and wind field. The LiDAR system is installed on the roof of the School of Earth and Space Science (SESS) building of the University of Science and Technology of China (USTC) in Hefei, Anhui province (Fig. S1a). This system operates at 1.5 μm eye-safe wavelength and uses 300 μJ pulse energy and 10 kHz repetition rate to achieve a maximum detection range of up to 15 km. The backscattering intensity and radial wind speed are set at the temporal resolution of 1 s and varying spatial resolution of 30/60/150 m, in order to improve the detection probability in the far-field where the signal is weak. The scanning range of the LiDAR can cover the upper hemispherical space with azimuth angle of 0–360° and zenith angle of 0–90°. The key parameters are listed in Table S2. Detailed information about the validation and application of the LiDAR system can be found in our previous works (Jia et al., 2019; Wei et al., 2019, 2020, 2021).

During the long-term observing period, the LiDAR system was set to operate in the velocity azimuth display (VAD) scanning mode with a fixed elevation angle of 60° and azimuth angle ranging from 0° to 300°. The scanning interval is 5° and a total of 60 radial profiles are obtained for each scanning circle, lasting 135 s. Then, the horizontal wind speed, wind direction, and vertical wind speed are retrieved from the measured radial speeds at different azimuth angles, based on the assumption of horizontally homogenous wind field (Smalikho, 2003; Banakh et al., 2010). Here, the wind direction of 0° represents the horizontal wind coming from the north, and the angle increases clockwise. Negative values of the vertical wind velocity indicate updraft.

The carrier-to-noise ratio (CNR) is usually used to describe the received signal intensity in the coherent Doppler lidar (CDWL) equation, which is defined as the ratio of the signal power to the noise power integrated over the detection bandwidth (Frehlich, 1996; Chouza et al., 2015). As a problem inherent to all single-wavelength lidars, the solution of the lidar equation requires the assumption of a lidar ratio and a boundary value, which may introduce large uncertainties to the retrieved aerosol extinction or backscattering coefficients. Due to the longer wavelength of CDWL systems, the aerosol extinction term is generally small, and the backscattering term dominates the CNR profiles. Therefore, the attenuated backscattering coefficient is preferred to be retrieved and applied for aerosol layer detection (Hirsikko et al., 2014; Wiegner et al., 2014). Here, the attenuated aerosol backscatter coefficient (β) is calculated by using a semi-qualitative calibration method from CNR (Huang et al., 2021; Pentikäinen et al., 2020; Wei et al., 2022).

$$\beta(R) = C\frac{CNR(R)^{*}R^{2}}{T_{f}(R)} \tag{1}$$

where R is range (distance from the LiDAR to the target), C is a constant calibration factor and derived by the integration of the backscattered signal over the optically thick, non-drizzling stratocumulus which can totally attenuate the laser energy (O'Connor et al., 2004), $T_f(R)$ is the focus function which is retrieved from horizontal scanning results by assuming that the aerosol distribution is homogeneous (Yang et al., 2020a).

In this study, we estimated the turbulent kinetic energy dissipation rate (TKEDR) by the turbulence statistical model with the relation between the structure-function of measured radial velocity and theoretical value (Banakh et al., 2017). The mixing layer height (MLH) is a significant parameter for measuring the vertical turbulent exchange within the ABL. We calculated the MLH at each time step by setting the specific threshold of TKEDR with a value of 10^{-4} m^2 s^{-3} (Banakh et al., 2021; Wang et al., 2021).

2.3. Meteorological and air quality data

The ambient air quality data are open accessed from the National Real-Time Air Quality Reporting System of the China National Environmental Monitoring Center (http://www.cnemc.cn/, last access: 25 March 2024). It should be noted that $PM_{2.5}$ and PM_{10} concentrations were comprehensive values from measurements based on multiple air quality monitoring stations in Hefei in this study. The specific locations of all monitoring stations can be found on the official website (https://aqicn.org/city/hefei/, last access: 25 March 2024). The nearest air quality monitoring station is located on Changjiang Middle Road (31.852°N, 117.25°E) and is ~2.7 km northwest to the LiDAR system. The real-time meteorological parameters, including air temperature and relative humidity, are obtained from an automatic weather station (Davis, Wireless Vantage Pro2 Plus). It is co-located with the LiDAR system on the roof of the School of Earth and Space Sciences building at the University of Science and Technology of China (USTC, 31.84°N, 117.26°E). This study also used ERA5 reanalysis data to interpolate the vertical profile of air temperature. ERA5 is the fifth generation ECMWF reanalysis for the global climate and weather on single levels from 1940 to the present. It provides hourly estimates for large numbers of atmospheric, ocean-wave, and land-surface quantities with a 0.25° by 0.25° regular latitude-longitude grid (https://cds.climate.copernicus.eu/cdsapp#!/dataset/reanalysis-era5-pressure-levels?tab=overview, last access: 25 March 2024).

2.4. Backward trajectory analysis

Backward trajectory analysis was conducted by using the Hybrid Single-particle Lagrangian Integrated Trajectory (HYSPLIT) model. HYSPLIT model is developed by the Australian Meteorological Agency and the National Oceanic and Atmospheric Administration (NOAA) to quickly simulate the dispersion and trajectory of substances that are transported and dispersed through the atmosphere (Draxler and Hess, 1998). The meteorological field of HYSPLIT model is driven by the National Centers for Environmental Prediction (NECP) operational Global Forecast System which analysis and forecast grids are on a 0.25° by 0.25° global latitude-longitude grid (http://www.ftp.ncep.noaa.gov/data/nccf/com/gfs/prod/, last access: 25 March 2024). We utilized an online HYSPLIT model to track the movement direction of air particles carried by the airflow and simulated the three-dimensional backward trajectory of airmass at the target area.

3. Results

3.1. Seasonal and diurnal profile of β and winds

This section analyzed seasonal and diurnal characteristics of aerosol vertical structure and meteorological conditions. Fig. 1 (a-c) depicts the seasonal profiles of β, horizontal wind speed, and vertical wind velocity below 3 km based on 3 years of Doppler wind LiDAR observations in Hefei. The results clearly showed that the maximum value of β appeared near the surface level among all seasons and gradually decreased as the altitude increased to the upper ABL. It should be noted that a sharp decrease of β at the lowest range gate was not an actual atmospheric phenomenon, but an artifact caused by the optical receiver system that attenuated the received backscattered signal. The vertical distributions of horizontal wind direction at different altitudes were presented as statistic frequency (%) in Fig. 1(d-g) in each season.

It was noticeable that the vertical β value in winter experienced the largest decrease along with altitude although the horizontal wind speed was lowest below 1.2 km. It could be explained by the following three reasons. First, the weaker horizontal wind and vertical diffusion contributed to stagnant air conditions that were conducive to the accumulation of pollutants within ABL in winter. Second, the turbulent mixing process caused by solar radiation was weaker in winter such that air pollutants could hardly be dispersed vertically. Furthermore, the predominant east wind within the ABL would cause transboundary air pollution, which sources were from the YRD region. Finally, long-range transport associated with the prevailing northwest wind in the upper atmosphere (>2 km) could bring about substantial air pollutants from northern China and aggravate surface pollution through downward transport.

In general, the vertical β was the lowest in summer than that in the other seasons within the ABL. It was due to both relatively large horizontal wind speed and vertical wind velocity. Wind conditions were favorable for better pollution diffusion and contributed to improve air quality in summer. In addition, the prevailing east wind in summer would bring warm and moist air masses. And it was favorable for the precipitation process as well as the wet deposition of aerosol. In spring, strong upper wind (>1.5 km) could advect high concentrations of transboundary dust particles to Hefei, due to the frequent dust events occurred in northern China. The phenomenon resulted in the largest β above 1.5 km in spring. In the lower ABL (<0.5 km), prevailing south wind (>5 m/s) and weak vertical wind velocity could lead to large values of β. Because the wind conditions were conducive to the transport and accumulation of anthropogenic source of aerosols from industrialized areas.

In terms of associations between β and the wind field at different heights, it was found that the faster the horizontal wind speed increases, the greater the decrease in β. In other words, the characteristic of vertical β above ABL was highly dependent on the upper-level wind speed,

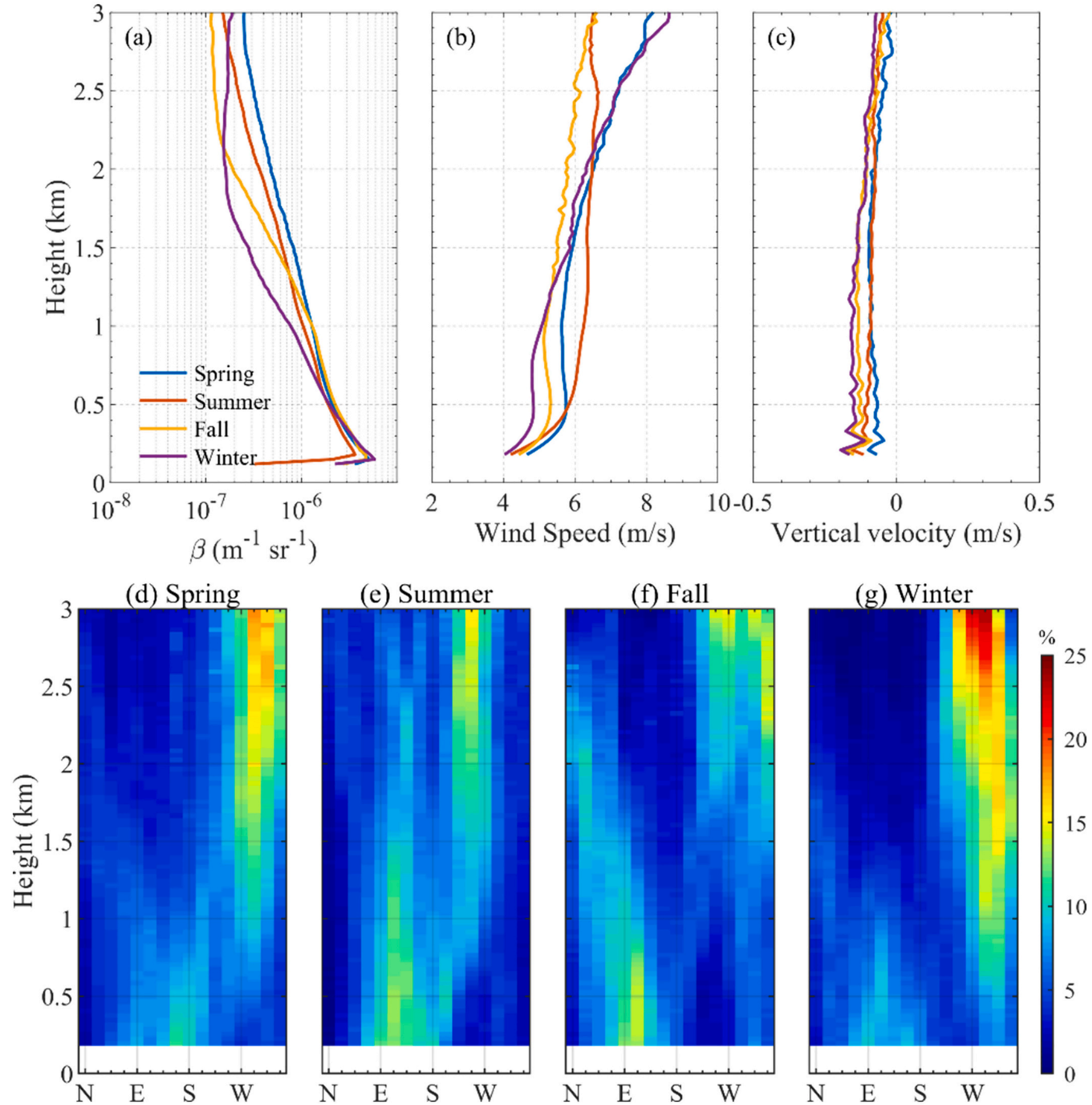

Fig. 1. Seasonal profiles of (a) β (m^{-1} sr^{-1}), (b) horizontal wind speed (m/s) vertical wind velocity (m/s), and horizontal wind direction frequency (%) within 3 km above ground in (d) spring, (e) summer, (f) fall, and (g) winter, respectively, at different heights (km). It is noted that the negative (positive) value of vertical velocity refers to the rising (descending) motion in the atmosphere in (c). The sum of each row equals 100% in (d-g). Spring: Mar-May; Summer: Jun-Aug; Fall: Sep-Nov; Winter: Dec-Feb.

as it could provide a better/worse horizontal diffusion condition. Furthermore, the predominant northwest wind with large horizontal wind speed in the upper air (> 2 km) in winter and spring would lead to transboundary air pollution and slow down the rate of descent of β, accordingly.

Taking into account the installation location of the Doppler wind LiDAR system and its blind zone, we retrieved the average vertical β at a height of 300 m (hereafter denoted by β@300 m) to represent aerosol characteristics in the near-surface layer. The diurnal variations of β@300 m and surface PM_{10}($PM_{2.5}$) concentration showed significantly positive associations between them (Fig. 2a). Fig. 2b shows the vertical spatial distributions of log-scaled β and the ABL height. Fig. 2c shows the vertical velocity variance (m^2 s^{-2}), which represents the intensity of turbulent structures in the boundary layer of mixing. Values of β within 1 km were relatively higher in the day (08:00 a.m. ~ 19:00 p.m.) than that in the night (20:00 p.m. ~ 07:00 a.m.), which was consistent with diurnal variations of the ABL.

In general, the hourly distribution of the surface PM_{10}($PM_{2.5}$) concentration exhibited two ‘humps’ pattern while β@300 m has the characteristics of a peak. In the morning, the surface PM_{10}($PM_{2.5}$)

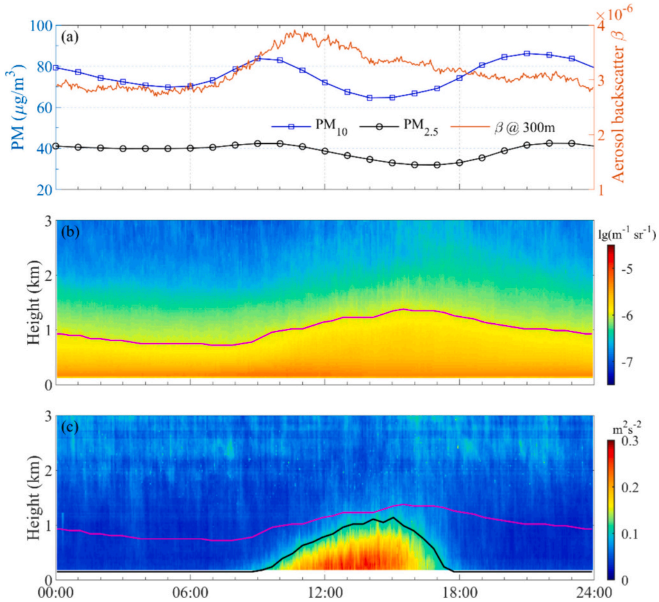

Fig. 2. Diurnal profiles of (a) $PM_{2.5}$, PM_{10} concentration (μg/m^3), and β@300 m (m^{-1} sr^{-1}), (b) logarithmic scaled vertical β recovered (m^{-1} sr^{-1}) at different heights (km), and (c) vertical velocity variance (m^2 s^{-2}) at different heights (km). The red line in (b) and (c) refers to the ABL (km), while the black line in (c) refers to the MLH (km). (For interpretation of the references to colour in this figure legend, the reader is referred to the web version of this article.)

concentration increased due to substantial sources of anthropogenic emission from human activities starting at the morning peak hour (06:00 a.m.). The average surface PM_{10}($PM_{2.5}$) concentration reaches a peak after the morning peak hour (09:00 a.m.). Later, the value gradually decreased due to strong vertical dispersion with the development of a solar-induced convective mixing layer. Therefore, the diurnal variation of the surface PM_{10}($PM_{2.5}$) concentration exhibited an opposite trend to the temporal evolution of the ABL height. After sunset, the surface PM_{10}($PM_{2.5}$) concentration began to increase due to the local accumulation of anthropogenic aerosols after the evening peak (21:00 p.m.) and reduced again after midnight due to dry deposition.

The value of β started to increase (decline) as the sun rises (sets), consistent with the diurnal evolution of turbulence intensity. However, the maximum value of β@300 m appeared at 10:00 a.m. and continued to decrease until the next morning. Compared to the surface PM_{10}($PM_{2.5}$) concentration, two hours' lag in the peak time of β@300 m might be caused by a delay in the upward transport of the surface layer. At night, the disappeared turbulent activities would prevent the vertical transport of aerosols from the surface to the upper air, resulting in continuous decreases in β@300 m. Therefore, it was worthwhile to specifically investigate the spatiotemporal characteristics of β and wind profiles by selecting typical HPEs to fully understand the formation and transport mechanism of air pollution in and above the ABL.

3.2. *Identification of typical HPEs*

It was necessary to firstly have a general understanding of seasonal and diurnal profiles of aerosol and winds based on 3-year LiDAR observations. In this section, we identified 12 typical HPEs to further investigate the mechanisms of the pollution process as well as the meteorological drivers. The specific standard to determine a heavy pollution episode (HPE) was using a threshold of hourly average PM_{10} concentration which exceeded 150 μg/m^3 for >6 consecutive hours. Hourly average PM_{10}($PM_{2.5}$) pollutants' concentration, relative humidity (RH), and β@300 m in each HPE were described in Fig. 3. Furthermore, it was found that most HPEs were associated with large-scale and higher values of aerosol optical depth (AOD). The spatial distributions of AOD in PM_{10} peak day were obtained from Moderate Resolution Imaging Spectroradiometer (MODIS) collection 6 (C6) Multi-angle Implementation of Atmospheric Correction (MAIAC) 1 km resolution AOD products (MCD19A2) in Fig. S3. From the point of view of satellite observation, some HPEs were closely correlated with strong cold front weather accompanied by thick cloud coverage. It should be noted that the LiDAR maintenance period (Table S1) was excluded in this study.

In Table 1, details of each HPE and its associated surface synoptic pattern are fully illustrated. We calculated the value of peak $PM_{2.5}/PM_{10}$ ratio in each HPE to imply extra information of aerosol type. The mass ratio was undoubtedly smaller than 1 and relatively lower values were observed in some HPEs. The duration time was longer than 12 h in all HPEs except EP8 (~6 h). In terms of HPEs (EP3, EP6, EP7, EP9, and EP12) with lower peak $PM_{2.5}/PM_{10}$ ratio (<0.18), cold air masses were driven southward associated with low RH and strong winds. The peak PM_{10} concentrations were 524 μg/m^3, 411 μg/m^3, 372 μg/m^3, 410 μg/m^3, and 578 μg/m^3 in EP3, EP6, EP7, EP9, and EP10, respectively. These HPEs were mainly dominated by PM_{10} pollution and related to outbreaks of dust events in January, March, and April. Meanwhile, our observations were consistent with statistical analysis of monthly atmospheric weather reported by National Meteorological Center (Mai et al., 2021; Mai and Zhang, 2022; Xu et al., 2021; Zhou and Zhang, 2020). Several dust-related HPEs were characterized by large peak PM_{10} concentration, which were 384 μg/m^3, 241 μg/m^3, 243 μg/m^3, 316 μg/m^3 in EP1, EP4, EP8, and EP10, respectively. Moreover, the size distributions of aerosol were observed to have a shift to larger particles in these HPEs. Our identifications of the above HPEs were also consistent with previous studies (Hu and Dong, 2021; Hua et al., 2021; Nie and Gao, 2021; Wang et al., 2020). Here, it should raise our concern about the outbreaks of dust events in Autumn (EP1 and EP4). Additionally, some HPEs (EP2, EP5, and EP11) had both large maximum PM_{10} (>140 μg/m^3) and peak $PM_{2.5}$ (>170 μg/m^3) concentrations which were related to winter fog-haze events. The identifications of the above HPEs were supported by studies from the National Meteorological Center (Chi et al., 2021; Nan et al., 2022; Zhang et al., 2020b). Stagnant weather conditions, such as weak surface winds and temperature inversion, were important influential factors for fog-haze weather formation and persistence.

It was reported that northern China had experienced large-scale and severe sand and dust storms in the same period as in EP9 and EP12. Therefore, it was worth evaluating the effects of sand and dust storms in the source areas on air quality in Hefei, since it is located in the downwind areas along the long-range transport pathway. Note that EP7 occurred at the end of a large-scale fog-haze episode in the YRD region during 20–28 January 2021. As a surface cold front extended south and east, strong northerly wind caused a termination of a fog-haze episode and a burst of a blowing sand event in the meantime. The pollution process in EP8 was special and originated mainly from anthropogenic emissions when it occurred during the Chinese Lunar New Year period. The intense discharge of fireworks from the lower ABL would aggravate PM_{10} pollution in EP8.

Therefore, we characterized all HPEs into the dust-related type and the fog-haze type according to the above characteristics of pollution process and weather system. According to Fig. 3, the higher PM_{10} concentrations in dust-related HPEs usually corresponded to relatively lower RH, while vice versa in fog-haze HPEs. Even for the same type of HPEs, it was worthwhile investigating the differences in pollution levels and the corresponding local meteorological conditions influenced by large-scale atmospheric circulation. The spatial maps of the near-surface synoptic analysis in PM_{10} peak day of each HPE were shown in Fig. S2. Regarding dust-related HPEs, two major types of synoptic patterns that influences air quality in Hefei were the Mongolian cyclone and the surface cold front system. Due to a blocking influence from the Dabie Mountains in the west of Hefei and mountainous areas in the south of Hefei, the prevailing wind direction from north and northwest would

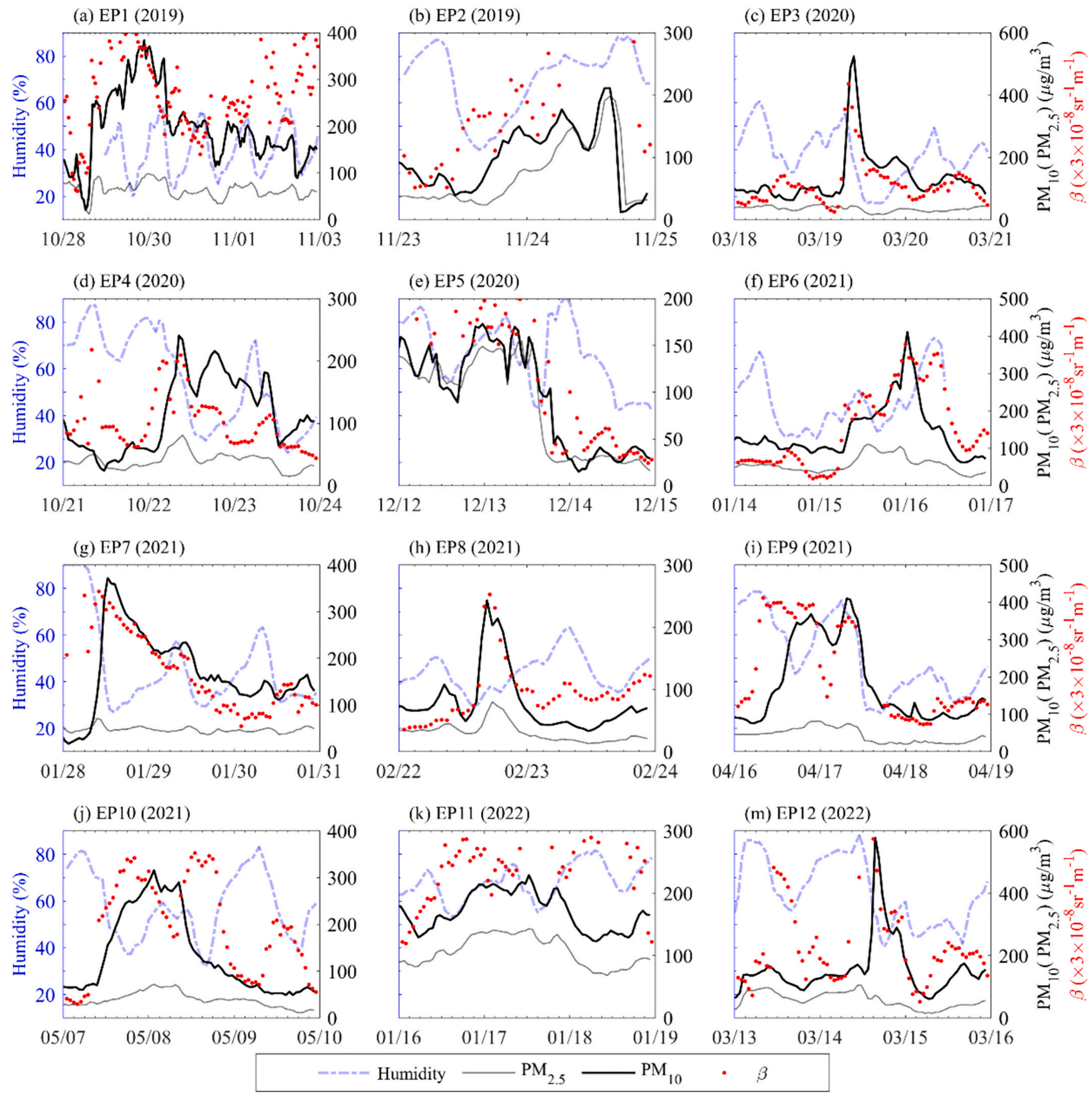

Fig. 3. Hourly average β value at 300 m height, surface PM_{10} and $PM_{2.5}$ concentrations, and surface relative humidity around the LiDAR station in each HPE. The gray line refers to hourly concentration of $PM_{2.5}$ while the thick black line represents hourly concentration of PM_{10} in each HPE. The red dot refers to β, and blue dotted line refers to relative humidity. Note that the β values during EP2 were two orders of magnitude higher than those of the non-episode so that the red dots were outside the upper bound of (b). (For interpretation of the references to colour in this figure legend, the reader is referred to the web version of this article.)

contribute to long-range transport of dust particles and exacerbate air pollution through downdraft and dust touchdown. For all fog-haze HPEs, surface synoptic conditions could be generalized as: equalized pressure field at the front of cold high-pressure system in EP2, at the base of high-pressure system in EP5, and weak high-pressure ridge system in EP11, respectively. The favorable weather conditions featured weak pressure gradients and wind speeds. Air quality was not only closely correlated with surface synoptic conditions, but also was affected by upper-level atmospheric conditions. Therefore, vertical profiles of aerosol and winds with high-time resolution were further explored based on long-term LiDAR observations in the next section.

3.3. Analysis of LiDAR observations during HPEs

In this section, we calculated one-minute average log-scaled β (m^{-1} sr^{-1}), 5-min average TKEDR, and 5-min average horizontal velocity at different heights to fully analyze the complex vertical structure of ABL during 12 typical HPEs. Figs. 4~6 show the time-height plots of the above vertical parameters retrieved from Doppler wind LiDAR observations. By comparing temporal changes between surface PM_{10}($PM_{2.5}$) concentrations and β (Fig. 3 and Fig. 6), it was found that β values always started to strengthen(attenuate) clearly when an episode started (ended). Importantly, temporal variation in PM_{10} concentration and β

Table 1

Illustration of typical HPEs and related meteorological information in Hefei from September 2019 to August 2022. Note that DUR, RH and TEMP refer to the total duration hours of each episode, surface relative humidity, and surface air temperature around LiDAR station, respectively.

Episode	Peak day (dd/mm/yyyy)	Peak time	DUR (h)	$PM_{2.5}/PM_{10}$ (μg/m^3)	RH (%)	TEMP (°C)	Surface synoptic patterns
EP1	29/10/2019	22:00	114	90/384	35	19.5	Mongolian cyclone and surface cold front accompanied by prevailing northwest wind was related to large-scale floating dust and blowing sand event.
EP2	24/11/2019	15:00	12	191/211	77	13.6	Equalized pressure field at the front of cold high-pressure was favorable for fog-haze event.
EP3	19/3/2020	10:00	18	44/524	32	18.1	Surface cold frontal passage accompanied by prevailing north wind was related to blowing sand event.
EP4	22/10/2020	09:00	28	76/241	58	17.2	Mongolian cyclone and surface cold high-pressure accompanied by northerly wind was related to floating dust event.
EP5	13/12/2020	00:00	14	149/173	75	8.1	At the base of high-pressure system, stagnant weather conditions during the interval between two cold air masses were favorable for fog-haze event.
EP6	16/1/2021	01:00	26	71/411	45	5.0	Mongolian cyclone and surface cold front accompanied by prevailing northerly wind was related to blowing sand event.
EP7	28/1/2021	13:00	36	46/372	61	9.9	Mongolian cyclone and surface cold front accompanied by northerly wind was related to blowing sand event.
EP8	22/2/2021	17:00	6	63/243	62	9.8	Surface cold frontal passage and low-level jet stream was related to blowing sand event.
EP9	17/4/2021	08:00	28	75/410	68	15.4	Mongolian cyclone and surface cold front accompanied by strong northerly wind was related to dust storm event in northern China.
EP10	8/5/2021	02:00	24	72/316	56	21.6	Mongolian cyclone and surface cold front accompanied by strong northerly wind was related to floating dust event.
EP11	17/1/2022	13:00	39	143/229	63	10.9	Stagnant weather condition influenced by weak high-pressure ridge was conducive to fog-haze event.
EP12	14/3/2022	16:00	17	73/578	53	20.9	Mongolian cyclone and surface cold front accompanied by strong northerly wind was related to dust storm event in northern China.

showed a good agreement during high PM_{10} concentration (>150 μg/m^3) period. In most HPEs (except EP5), elevated PM_{10} concentration was associated with a high TKEDR value within the mixing layer (ML). It indicated an important role of strong vertical turbulence with a high vertical velocity (Fig. S4) in pollution accumulation. In EP5, an increase in $PM_{2.5}$ concentration started in the afternoon and reached a peak at midnight under the background of large-scale fog-haze episodes in the YRD region. The air pollution process in EP5 could be explained by stagnation in air and high relative humidity which favored the hygroscopic growth of particles in winter. Furthermore, we found that the maximum concentration of PM_{10} was always accompanied by a sudden change in the direction of the surface wind. For example, EP2, and EP7 were associated with northwest wind; EP3, EP4, EP6, EP8 and EP12 were associated with northeast wind; EP9, EP10, and EP11 were associated with north wind. Since there were 9 dust-related events in total, we would like to discuss them more clearly by clustering them into two groups based on the $PM_{2.5}/PM_{10}$ ratio with a threshold value of 0.2. Group I (Group II) referred to the HPEs in which the ratio is smaller (larger) than 0.2. In consequence, Group I included EP3, EP6, EP7, EP9 and EP12. Group II included EP1, EP4, EP8 and EP10.

As for dust-related HPEs in Group I, the occurrence of HPEs was prevalent in spring and winter. In each HPE, the diurnal trend of the surface PM_{10} concentration was highly consistent with β@300 m(Fig. 3). Fig. 4c shows a notable dust event according to the vertical structure of β in EP3. During the whole period, the temporal variation in vertical distributions closely corresponded to the evolution of MLH as well as vertical mixing (Fig. 5c). Before EP3, horizontal winds became strong and gusty within ML and later in the upper air. The upper wind at the top of ML shifted sharply to the northeast direction from ~4 h before peak time as cold front passed by (Fig. 6c and Fig. S5c). The weather situation favored long-range transport of dust particles from distant source regions, for example, deserts in western and northwestern China. At the beginning of EP3, the higher values of β (>10^{-5} m^{-1} sr^{-1}) mainly concentrated below the lower ML (< 0.3 km) which corresponded to an increase in wind speed during this period. On a peak day from 12:00 p.m. to 21:00 p.m., an explicit downward transport belt was found above the ML (~1.5 km). Meanwhile, aerosols below and above ML were mixed with the evolution of ML. In the end, surface PM_{10} pollution was cleared by a sudden change of prevailing wind direction from north to east. In EP6, large β (>10^{-5} m^{-1} sr^{-1}) values are mostly distributed within the ML (<0.3 km) in Fig. 4f. At the beginning of EP6, a notable downward transport of aerosols from the upper air (~ 2.5 km) to the surface layer was witnessed. Additionally, increasing aerosol concentrations from 21:00 p.m. on 15 January to 3:00 a.m. on 16 January were due to a strong low-level jet stream above the ML (~0.5 km). Strong horizontal wind below 1.5 km and intense vertical mixing contributed to a relatively higher MLH at night. Before peak time, an increasing PM_{10} concentration associated with a decreasing $PM_{2.5}$ concentration was discovered. It implied that long-range transport of large aerosol particles contributed the most to surface PM_{10} pollution. While several hours after the peak time, hygroscopic growth of aerosol was observed that caused large values of β in the near-surface layer (Fig. 3f). Regarding the vertical distributions of β and wind profiles in EP7, it was found that aerosol particles with large β (>10^{-5} m^{-1} sr^{-1}) mostly concentrated in the lower ML (<0.3 km) before sunset on peak day (i.e., 28 January 2021 in Fig. 4g). In regard of air pollution, the surface PM_{10} concentration reached a peak at noon on a peak PM_{10} day and began to decline due to an abrupt change of the surface prevailing wind direction from north to south. With the evolution of MLH, the vertical distributions of large β are still suspended in the range between 0.3 km and 0.2 km at night. It suggested an important role of the near-surface jet stream in blowing local aerosol sources into the upper air. In the morning (~9:00 a.m.) on 29 January 2021, a weak low-level jet stream with a horizontal wind speed >5 m/s (centered at a height of 0.4 km in Fig. 6g) led to a small peak of PM_{10} concentration (Fig. 3g).

The pollution process characterized by the vertical β and wind profiles in EP9 was similar to that in EP3. In comparison, the total duration hours of EP9 were longer than that of EP3 while the MLH in EP9 was much lower than that of EP3. Moreover, vertical distributions of large β (>10^{-5} m^{-1} sr^{-1}) mainly concentrated within the ML at night (Fig. 4i). Later, these particles gradually deposited and accumulated to the near-surface layer. With the development of a strong north wind after sunrise, long-range transport of aerosol particles mixed with local aerosol in the ML. It led to the peak PM_{10} concentration at 08:00 a.m. EP12 represents a severe dust-storm event in northern China on 14 March 2022. During the period, the maximum concentration of PM_{10} was 578 μg/m^3 in the afternoon (16:00 p.m.). Before EP12, intense cloud coverage was explored in a range of 1.5 km ~ 2 km (Fig. 4m) accompanied by strong

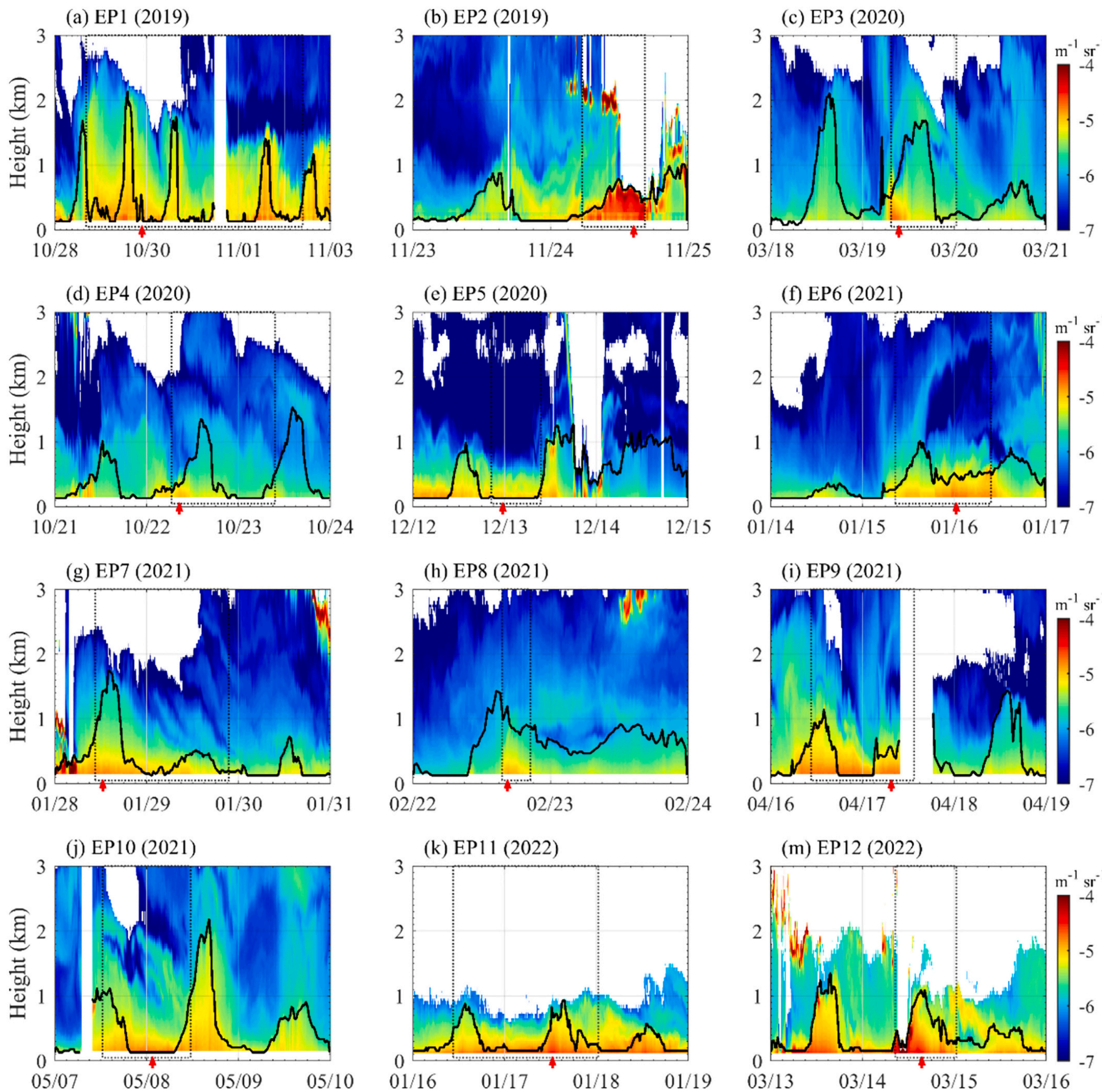

Fig. 4. Time series of a one-minute average log-scaled β (m^{-1} sr^{-1}) at different heights (km) during each HPE. Note that the gray dotted box represents the total duration time, the black line represents MLH, and the red arrow refers to the peak time of PM_{10} concentration in each HPE. (For interpretation of the references to colour in this figure legend, the reader is referred to the web version of this article.)

northeast wind (>10 m/s) below 2 km. At the beginning of EP12, it should be noted that the received signal was sharply attenuated. It resulted in a decreasing detection range of the LiDAR systems and explained the nan values of β at ~12:00 at noon. With the development of MLH, aerosols were elevated to upper air (~1 km) by a strong northeast wind and large turbulence (Fig. 5m). Severe surface PM_{10} pollution was alleviated by an abrupt change in prevailing horizontal wind direction from northeast to east. It was noted that significant signals of cirrus clouds were detected above the lower troposphere (~1.5 km) before EP12 while the spatial map of AOD showed coverage of thick clouds over Hefei at peak PM_{10} day (Fig. S3m).

In terms of dust-related HPEs in Group II, they occurred in spring, autumn, and winter. EP1 referred to a long-lasting (114 h) blowing and floating dust in October 2019. In general, the vertical distributions of aerosols were mostly correlated with diurnal MLH, which depended on vertical atmospheric thermodynamic structure. In Fig. 4a, an obvious downward transport of aerosols from high-altitude (~2 km) to the near-surface layer was observed at the beginning of EP1. It was due to strong horizontal northwest wind (Fig. S5a) and downward wind (i.e., negative vertical wind speed in Fig. S4a). Before peak time, the horizontal soft wind was favorable to the accumulation of particle aerosols below the lower ABL (< 0.5 km) such that large β(>10^{-5} m^{-1} sr^{-1}) was discovered consequently. Influenced by a strong north wind in the upper air (>1.8 km) and a light south wind in the near-surface layer, the surface PM_{10} concentration reached a peak late at night. Due to an increasing southwest wind after peak time, particle aerosols were lifted and

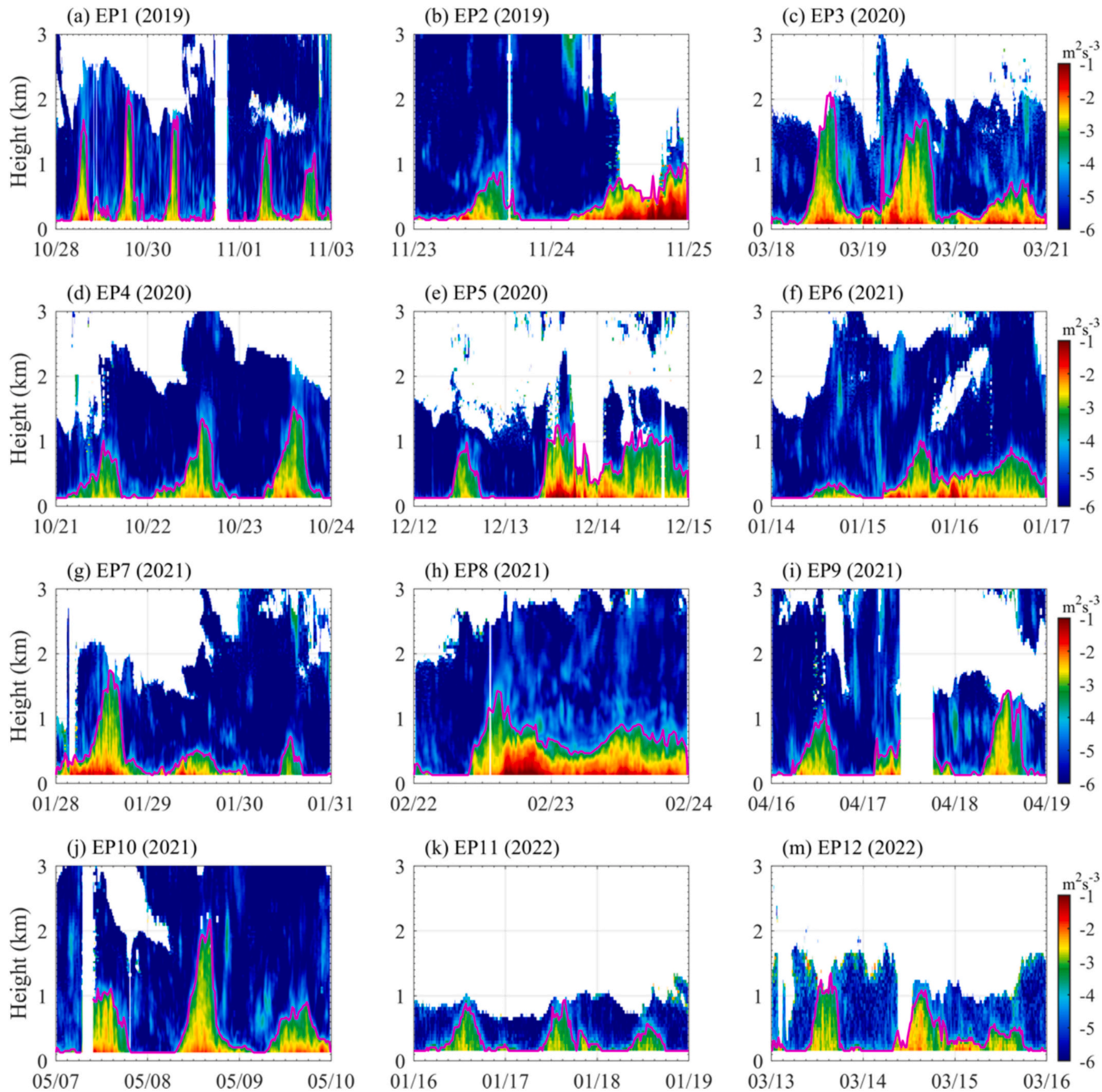

Fig. 5. Time series of 5-min average TKEDR ($m^2\ s^{-3}$) at different heights (km) during each HPE. Note that the magenta line represents the MLH in each HPE. (For interpretation of the references to colour in this figure legend, the reader is referred to the web version of this article.)

suspended below 0.5 km so that large β (>10^{-5} m^{-1} sr^{-1}) was found correspondingly. At the end of EP1, an obvious large lift of large β (>10^{-5} m^{-1} sr^{-1}) at a height of 0.8 km was caused by a sudden strong southwest wind. Diurnal variations of the surface PM_{10}($PM_{2.5}$) concentration were opposite to that of hourly RH at night. It could be explained by the regional transport of anthropogenic sources from urban/industrial areas in the near-surface layer. And it could contribute to significant changes in aerosol size distributions of the mixed aerosol particles and enhance the ability of light backscattering by aerosols. In terms of EP4, peak PM_{10} concentration appeared at the beginning while large β (>10^{-5} m^{-1} sr^{-1}) mostly located below 0.3 km and sustained for several hours (Fig. 4d). The surface PM_{10} pollution was attributed to a national cold air process that triggered a blowing sand event. The north wind in the upper air brought substantial aerosol particles. And the light wind in the near-surface layer (~0.2 km) was conducive to local accumulation from the beginning of EP4. The intense northwest wind in the upper ABL (> 2 km) contributed to the long-range transport of aerosols (β >10^{-6} m^{-1} sr^{-1}) such that we could obviously witness a distinction signal belt in the first half of EP4. The downward transport and mixing of aerosols took place within the ML. Taking into account the vertical β (< 10^{-5} m^{-1} sr^{-1}) several hours after the peak time, the corresponding lower β was caused by the dominant proportion of coarse particles. It was supported by a lower $PM_{2.5}$/PM_{10} ratio(Fig. 3d).

EP8 was regarded as a special episode of particle pollution during the Chinese Lunar New Year (CNY). The aerosol particles deposited derived from the intensive discharge of CNY fireworks were elevated to the

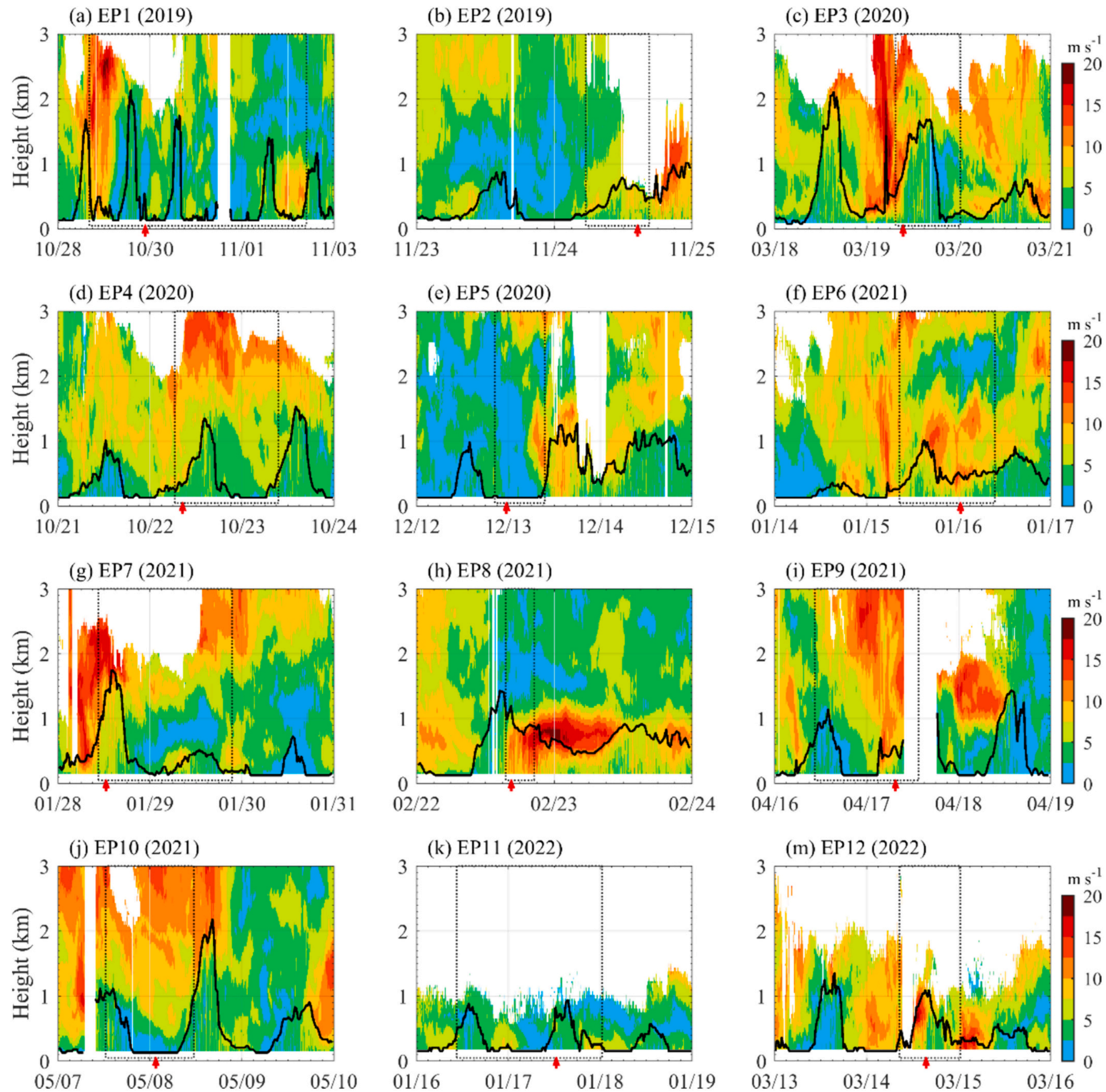

Fig. 6. Time series of 5-min average horizontal velocity (m/s) at different heights (km) during each HPE. Note that the black dotted box represents the total duration time, the black line refers to MLH, and the red arrow refers to the peak time of the PM_{10} concentration in each HPE. (For interpretation of the references to colour in this figure legend, the reader is referred to the web version of this article.)

upper air driven by a notable low-level jet stream (centered at a height of 0.7 km in Fig. 6h). We observed a distinct downward transport of large β ($>10^{-5}$ m^{-1} sr^{-1}) from the top of ML to the near-surface layer. The maximum PM_{10} concentration appeared in the afternoon as the surface horizontal wind became much stronger. With the rapid development of the low-level jet stream, particle pollution was quickly mitigated and β sharply reduced. EP10 referred to a typical dust event that took place in May 2021, which was associated with relatively higher solar radiation and vertical turbulence. Before EP10, a strong northwest wind above the ML contributed to the long-range transport of aerosol particles from the dust-source regions. From the beginning of EP10, we found a significant downward transport belt (β $>10^{-6}$ m^{-1} sr^{-1}) from the upper air (~2.4 km) to the ML (Fig. 4j). As the wind direction turned from northwest to southwest at night (Fig. S5j), the near-surface wind speed reduced sharply. The weak wind condition inhibited the ability to diffuse air pollution such that the surface PM_{10} concentration accumulated to a peak at 2:00 a.m. Furthermore, large β ($>10^{-5}$ m^{-1} sr^{-1}) concentrated in the near-surface layer (< 0.2 km) throughout the night. It resulted in a steady and high level of surface PM_{10} concentration (> 250 μg/m^3). Similarly to EP6, an increasing trend of β@300 m was found at the end of EP10 while hourly surface PM_{10} concentration decreased (Fig. 3j). It could be explained by that active solar radiation strengthened vertical mixing and hence accelerated changes in aerosol size distribution within the ML after sunrise.

During fog-haze HPEs (EP2, EP5, and EP11), surface RH was relatively higher than that in dust-related HPEs. In general, hourly variations of surface PM_{10}($PM_{2.5}$) concentration were in agreement with that of hourly RH before the peak time. In these HPEs, the higher $PM_{2.5}/PM_{10}$ ratio occurred under sub-saturated atmospheric conditions which favored hygroscopic growth of aerosol particles. Particularly in EP2, thick cloud signals (Fig. 4b) were observed from a height of 1.5 km to 2 km while large β ($>10^{-5}$ m^{-1} sr^{-1}) within ML were observed correspondingly in the former part of episode. It should be noted that a vertical distinction belt of β at the top of ML from 12:00 pm to 18:00 pm was present, highly associated with strong vertical turbulent mixing (Fig. 5b). Furthermore, the extremely large β ($>10^{-4}$ m^{-1} sr^{-1}) at the top of ML indicated signals of thick clouds and fog weather. Regional transport of particles and unfavorable weather resulted in severe $PM_{2.5}$/PM_{10} (191/211 μg/m^3 at peak time) pollution. At the end of EP2, β within the ML started to drop sharply due to precipitation (RH was almost 100%). In EP5, the vertical pattern of β profile (Fig. 4e) was not as significant as that in EP4. However, we could observe substantial aerosol particles that accumulated in the near-surface layer (< 0.2 km) before EP5. The entire pollution process occurred at night and reached its peak at midnight due to unfavorable meteorological conditions (i.e., shallow ABL, low wind speeds and high RH). The intensive aerosol

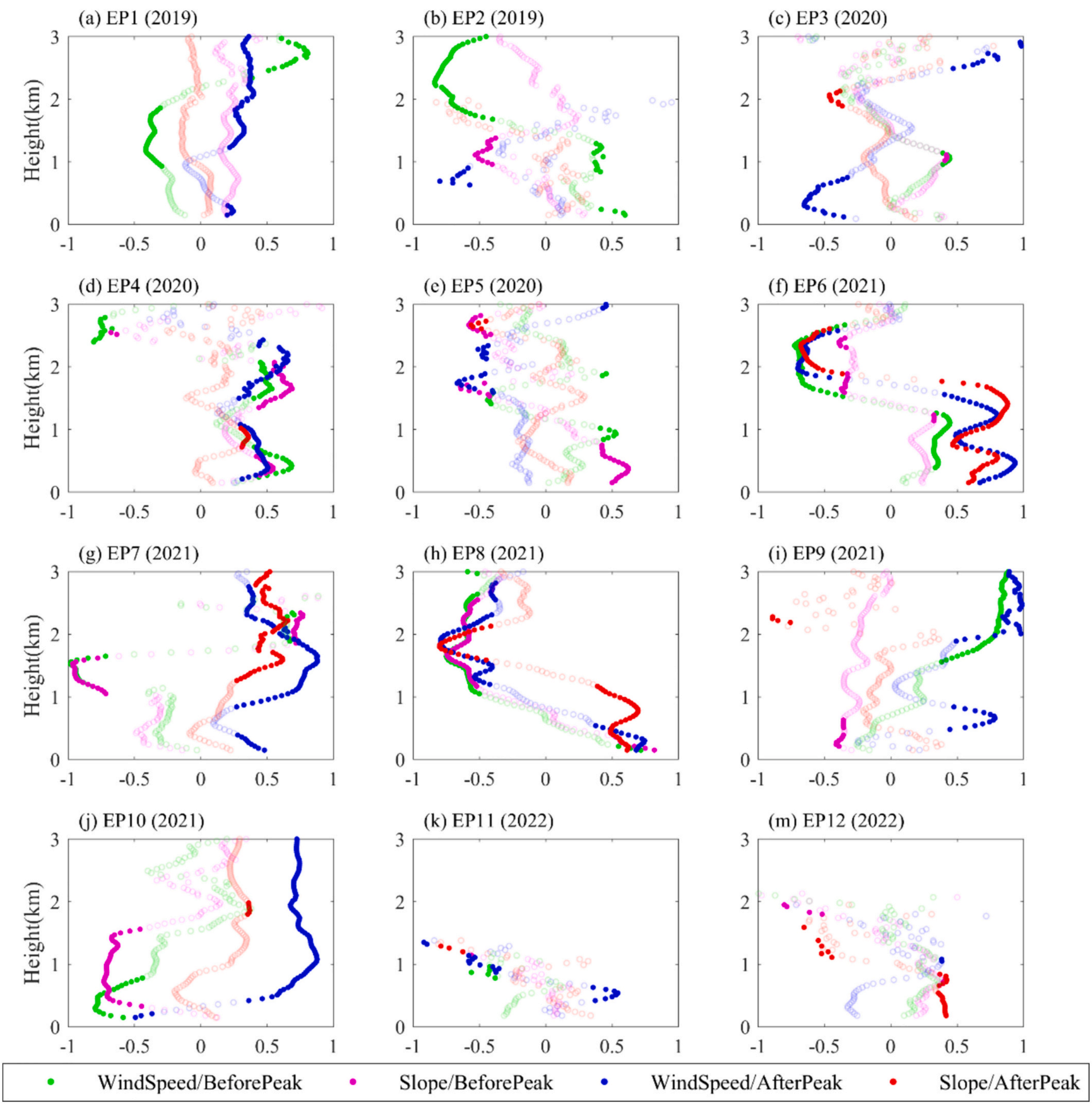

Fig. 7. Vertical distributions of correlation coefficients (x-axis) between horizontal wind speed at different heights (km, y-axis) and surface PM_{10} concentration during each HPE. BeforePeak represents 24 h before the peak PM_{10} time. AfterPeak represents 24 h after the peak PM_{10} time. Slope refers to the correlation coefficients between the gradient of changes in surface PM_{10} concentration and horizontal wind speed at different heights. Note that the filled circles indicate correlation significance passed the 95% confidence level.

particles were cleared when significant signals of snow condition along with strong northerly wind were detected. The spatiotemporal characteristics of particle pollution in EP11 were straightforward to understand. First, stagnant weather conditions were conducive to the formation of fog-haze episode. Second, the water vapor was absorbed by the aerosol particles under high RH and low visibility conditions (Table 1). It showed a good agreement between hourly PM_{10} concentration and RH in Fig. 3k. Finally, large β (>10^{-4} m^{-1} sr^{-1}) associated with high MLH and strong daytime turbulence was discovered (Fig. 4k). Surface PM_{10} concentration reached a peak at 13:00 p.m. due to local accumulation of substantial aerosol particles under weak wind conditions.

3.4. Role of horizontal winds at different altitudes on PM_{10}

In this section, we calculated the correlation coefficients (Φ) between hourly horizontal wind speed and hourly surface PM_{10} concentration (Fig. 7) at different heights to investigate how the vertical structure of winds affected the whole pollution process. Winds could not only clear surface aerosol particles but also carry transboundary air pollutants to downwind receptor areas. For a certain height, a large positive Φ value indicated that the higher wind speeds could exacerbate much more surface PM_{10} pollution whereas a negative Φ value meant the removal of PM_{10} pollutants by strong winds. Associations between the simultaneous hourly/1-h lag/2-h lag of surface PM_{10} concentration and hourly wind speed at different heights were also assessed in Fig. S6. Since the occurrence and development of dust-related HPEs were closely related to the invasion of cold air, we retrieved the vertical profile of atmospheric temperature from ERA5 reanalysis datasets and interpolated the grid to geographical coordinates of the LiDAR observing site in each HPE (Fig. S7). To comprehensively analyze the transport process of aerosol particles driven by winds at different heights, we further calculated the profile of air pollution diffusion coefficient (φ, Fig. S8) and performed backward trajectory analysis at various starting heights from peak PM_{10} time (Fig. 8 and Fig. S9) for each HPE, respectively. It was noted that a value of φ was calculated as the ratio of the frequency of wind direction in a receptor region to the average wind speed in that direction. The backward trajectories of air parcels at heights of the near-surface layer and the upper layer mainly originated from northwestern China and Mongolia in most dust-related HPEs. Additionally, the vertical profile of the air temperature before/after peak PM_{10} time (hereafter denoted as before/after peak) could reveal the moving process of cold air masses.

For HPEs in Group I, vertical characteristics of Φ varied episode from episode. Vertical values of Φ in EP3 below 0.8 km were significantly negative during 24 h after the peak (Fig. 7c). Moreover, a notable effect of time lag (2 h) on vertical Φ in the near-surface level and upper level (0.5–1.5 km) were discovered (Fig. S6c). Combining the results of vertical temperature profiles and backward trajectory analysis, we could conclude that strong winds made the major contributions to increasing surface PM_{10} concentration by long-range transport of aerosols at the upper level of the atmosphere and subsequently strong vertical transport to the surface during the whole episode. Note that negative values of Φ at heights below 0.8 km at 24 h before peak were not controversial with the above results because of the different hours included in the calculations. The period, i.e., 24 h before peak, was almost before EP3 during which the strong cold air masses started to influence the receptor area and alleviated surface PM_{10} pollution instantly. In contrast with EP3, significant positive values of Φ below 1.5 km during 24 h before and after peak were observed in EP6 (Fig. 7f). In terms of the whole episode, horizontal winds below 1.5 km were conducive to the enhancement of surface PM_{10} concentration (Fig. S6f). It highlighted the long-range transport of aerosol pollutants which might serve as the main influential factor for surface PM_{10} pollution. However, an opposite distribution of vertical Φ values was noticed in the upper air (> 1 km). Positive correlation between horizontal winds in the near-surface layer (< 0.3 km) and surface PM_{10} concentration during 24 h before peak was particularly observed in EP7 (Fig. 7g). In comparison, negative values of Φ were only significant between ~0.4 km and ~ 1 km for the entire episode (Fig. S6g). The results made it clear about the different roles of horizontal winds at different atmospheric layers. The near-surface soft winds conduced to local accumulation while the upper-level winds were beneficial to surface pollutant abatement. In EP9, positive correlations between horizontal wind speeds and surface PM_{10} concentration were significant at the upper ABL (0.5–0.9 km) during 24 h after peak, which corresponded to vertical patterns of horizontal winds. Similarly, large positive values of Φ were observed above 2 km due to the influence of strong winds. In EP12, the contributions of horizontal winds in 1-h/2-h lag to surface PM_{10} concentration were significant between ~0.5 km and ~ 1.3 km. The origin of the near-surface (~0.5 km) backward trajectory overlapped with trajectory at a starting height of 1.5 km and was close to our LiDAR station in Hefei. It indicated that strong upper winds carried substantial aerosols from northwestern China and consequently affected surface PM_{10} concentration due to intense vertical turbulence and regional transport in the near-surface layer.

As for HPEs in Group II, the general pattern of Φ profile showed significant positive correlations between horizontal winds below 1 km and surface PM_{10} concentration during 24 h after peak. In EP1, we observed an opposite role of vertical wind profile on surface PM_{10} pollution 24 h before/after peak (Fig. 7a). The obvious air temperature dropped with altitude and significant negative values of Φ above 1 km were found. It indicated that strong cold air masses associated with large wind speeds in the upper air would clear the air at the beginning but later contributed to raising surface PM_{10} levels through regional transport in the near-surface level and through downward transport of aerosol particles from the upper air. In terms of total duration hours (114 h) in EP1, horizontal winds made an overall negative contribution to the surface PM_{10} concentration below 1 km because the wind speeds had been weakening from 13 h after the beginning. This finding was supported by the relatively lower φ values during the episode. In EP4, significant positive values of Φ below ~0.8 km and above 1.5 km were observed during 24 h before and after peak (Fig. 7d). The pollution process was affected by weather situation which a cold air mass clump of Lake Baikal was swept southward (Fig. 8d) such that a strong north wind below 2 km made dominant contributions to surface PM_{10} pollution 24 h before peak. The overall influence from horizontal winds at each height in EP4 (Fig. S6d) could be supported by vertical φ values (Fig. S8d). Winds below 0.5 km and above 1.5 km were positively correlated with surface PM_{10} concentration in EP4. Large negative values of Φ between wind speed (slope) at 1 km and surface PM_{10} pollution demonstrated a special role of the low-level jet stream in surface pollution in EP8 (Fig. 7h). The evolution of a low-level jet stream from the east direction provided favorable air pollution diffusion conditions (Fig. S8h). In EP10, significant Φ below 0.8 km illustrated negative impacts of northwest and west winds on surface PM_{10} concentration during 24 h before peak (Fig. S8j). Furthermore, the 500-m backward trajectory and weak wind speeds robustly distinguished EP10 as a blowing sand event. In the near-surface layer, dust particles mainly originated from the local and neighboring areas. High positive values of Φ above 1 km suggested transboundary pollution caused by northwest wind during 24 h after peak.

Accounting for the stagnant weather conditions that favored fog-haze formation, it was expected that most of vertical Φ values were insignificant below 1 km during 24 h before/after peak in EP2, EP5, and EP11. When looking at the whole episode, negative values of Φ were significant below ~2.8 km and Φ values in 1-h/2-h lag were discovered in EP5. The results highlighted the removal of air pollutants by strong northwest and north wind in the atmosphere. In particular, backward trajectories at starting heights below 1 km were much shorter in fog-haze HPEs compared to that in dust HPEs.

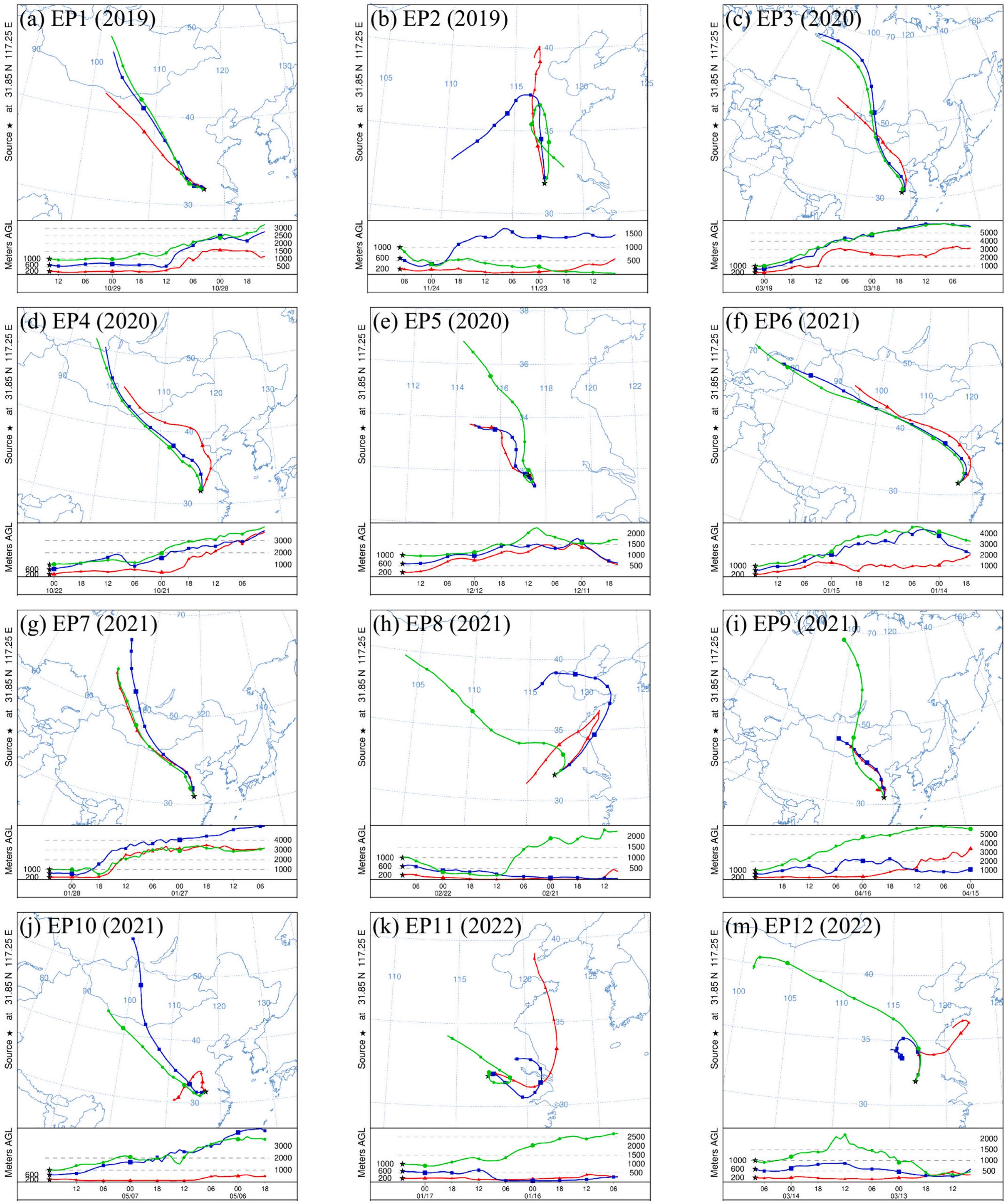

Fig. 8. Backward trajectory analysis at starting heights of 200 m, 600 m, and 1000 m in each HPE, respectively. The starting time of the backward trajectory analysis was from the peak PM_{10} time in each HPE.

4. Discussion and implications

A comprehensive and systematic understanding of how synoptic patterns influence the boundary layer structure of aerosol formation and transport requires not only ground-level measurements, but also high-spatiotemporal-resolution vertical profiles of aerosol and winds. Most of previous studies used the LiDAR system to monitor the air pollution process in ABL just for sporadic events. However, the lack of long-term air quality measurements in ABL could limit our full understanding of the temporal characteristics of transboundary pollution and thus the prediction of air quality. To our knowledge, this is the first study to analyze long-term Doppler wind LiDAR measurements for 3 years in Hefei, one of the three key cities in the YRD region. Furthermore, continuous observations in this study could expand previous LiDAR studies on conducting long-term detection of aerosol profiles in Hong Kong (Yang et al., 2019; Yim and Huang, 2023) rather than in mainland China.

Several previous studies just examined the HPEs (e.g., sand and dust storms) close to sand source areas/cities. In this study, we investigated the characteristics of different HPEs in a distant city, far from the dust sources for early warning of extreme weather events. An earlier study conducted LiDAR observations of four Asian dust events over Hefei in the spring of 2000 (Zhou, 2002). They characterized the different types of typical Asian dust extinction profiles. Here, our vertical observations of aerosol backscatter coefficient in dust-storm-related HPEs were consistent with Zhou (2002). The pathways of how Asian dust particles influenced local aerosol particles in Hefei could be characterized in two types: the first type increased large aerosol particles within the ML and then mixed with local aerosol particles due to strong vertical mixing; the second type was that elevated Asian dust layers mainly located between 1–3 km and intruded into Hefei above the ML. The finding was also confirmed in a recent study for Barcelona, a large metropolitan area in the Mediterranean region (Lolli et al., 2023). Among all types of dust events in China, floating dust events occurred the most frequently (Zhao et al., 2022). However, studies had seldom concentrated on pollution characteristics of floating dust episodes in the YRD region, not to say in Hefei in the western YRD region. With the available long-term observations of aerosol and wind profiles, this study identified 12 typical HPEs and analyzed their spatiotemporal characteristics during the pollution process. For example, we observed a particularly severe fog-haze episode (EP8) during CNY period in February 2021. It was highly associated with a strong low-level jet stream above the ML and affected by a surface cold frontal passage. During the episode, intense fireworks discharge in the lower ML ($<$ 0.2 km) blown up by strong winds caused surface PM_{10} pollution. It highlighted the necessity to comprehensively understand the differences between HPEs on account of weather system, pollution process, and the spatiotemporal characteristics of aerosol and winds at different heights.

The vertical distributions of aerosol particles at different heights were largely influenced by weather systems and meteorological conditions. Wind fields and atmospheric pressure strongly determined the predominant transport pathways of nonlocal particle pollutants. Since Hefei is located in eastern and central China, the level of air pollutants could be influenced by sources from any direction. Several studies focused on a typical polluted weather process in Hefei and determined the transboundary aerosol mainly from the northwest direction (Fang et al., 2021; Zhang et al., 2020c). It should be noted that large topography also had an impact on the regional atmospheric environment. For example, Zhao et al. (2023) highlighted the important role of vertical clockwise circulation on transporting air pollutants from the central and eastern Sichuan Basin to the eastern foothills of the Tibetan Plateau by southeasterly winds. In this study, a blocking influence from Dabie mountains in the west of Hefei could affect urban surface ventilation potential and atmospheric diffusion conditions. We also found that long-range transport of dust particles was always driven by north and northwest winds and aggravated surface air pollution through downdraft and dust touchdown.

This study complemented previous research by identifying and categorizing 12 HPEs into dust-related and fog-haze episodes. Note that dust-related HPEs in this study (visibility $<$10 km) included both blowing sand and floating dust weather events, which could be mainly differentiated by wind speed and source regions of dust particles. We further classified these dust events into two groups based on $PM_{2.5}/PM_{10}$ ratio to clearly assess the corresponding influences from winds at different altitudes on surface PM_{10} pollution. Previous studies pointed out that particulate transport from North China to East China was a common phenomenon influenced by the winter monsoon (Mao et al., 2022; Qin et al., 2016). This study made full use of in-situ vertical LiDAR observations, ambient air quality data, meteorological data, reanalysis data, and satellite data to clarify major transport pathways and different heights of transboundary or regional particle pollutants. Regarding the spring dust-related HPEs, it was found that the long-range transport of aerosol particles at higher altitudes ($>$1.5 km) originated from the northwest source region, driven by the Mongolian cyclone and the cold front system. While in the middle boundary layer ($\sim$0.5 km) for winter fog-haze events, potential source regions for transboundary aerosols were almost located in the northern part of Anhui province and the YRD region, which were supported by Hong et al. (2019).

Long-term observations of aerosol and wind profiles based on LiDAR systems with high-time resolution were definitely advantageous and beneficial for practical applications of regional air pollution monitoring. However, this study still had some limitations and uncertainties. First, there was inevitably a lack of data during long-term LiDAR observations due to extreme weather influences and occasional instrument maintenance. We counted the total effective data at different heights and times (Fig. S1). The statistical results showed the robustness and reliability of LiDAR datasets in this study. Secondly, the limitation of the Doppler wind LiDAR system was that it could only provide information on total aerosol backscatter and extinction coefficient, whereas lacking microphysics parameters. Therefore, we could not distinguish the specific type of aerosol. In the future, we will integrate the polarization function in the LiDAR system to provide aerosol-type identification. Finally, vertical measurements of a single-site LiDAR system would limit our knowledge about transboundary air pollution over cities. Therefore, we would establish a real-time LiDAR monitoring network to provide more systematic knowledge about transboundary air pollution in the next step.

5. Conclusions

This study conducted a 3-year consecutive Doppler wind LiDAR measurements in Hefei in western YRD region, China. We investigated the spatiotemporal characteristics of retrieved β and wind profiles from the perspective of long-term statistics and typical HPEs. The seasonal β profile showed a peak in the near-surface layer among all seasons and gradually declined as the altitude increased to the upper ABL. The overall β profile was highest in winter and lowest in summer below 0.5 km. In contrast, the β profile above the ABL had the highest reduction rate in winter which is associated with strong horizontal wind. In spring, an increasing occurrence of dust events with high upper-level wind contributed to the largest β above 1.5 km. The diurnal variation of β@300 m showed a peak at 10:00 a.m. while the surface PM_{10}($PM_{2.5}$) concentration exhibited two 'humps' pattern (peak at 09:00 a.m. and 21:00 p.m.). We identified 12 HPEs and classified them into dust-related (including dust storm, floating dust and blowing sand events) and fog-haze episodes. The results showed a consistent variation between hourly PM_{10} concentration and @300 m, particularly during a high PM_{10} concentration ($>$150 μg/m^3) period. In addition, the maximum PM_{10} concentration was always accompanied by a sudden change of surface wind direction. In the spring dust-related HPEs, the pollution process was mainly contributed by long-range transport of aerosol particles at upper altitudes ($>$1.5 km) from the northwest direction, driven by the Mongolian cyclone and cold front system. In winter fog-haze HPEs, hourly PM_{10}($PM_{2.5}$) concentration performed an agreement with hourly RH before peak PM_{10} time. Moreover, the transboundary aerosols in the middle boundary layer (~0.5 km) were mainly from the northern part of Anhui province and the YRD region. The correlation coefficients (Φ) between β and wind profiles were assessed to identify the different roles of horizontal winds at different altitudes and their associated time delay effect on surface PM_{10} pollution. Significant positive contributions from horizontal winds were observed in lower ABL (< 0.5 km) during the entire dust-related episode in EP4 and EP6, indicating that the higher wind speeds could exacerbate PM_{10} pollution. In contrast, large negative Φ values meant the removal of PM_{10} pollutants by strong winds below 0.8 km during 24 h after peak in EP3. The time delay of surface PM_{10} pollution at different heights was found in EP5 (< 1.5 km), EP6 (> 2 km), EP7 (> 1.8 km), EP8 (> 0.8 km), and EP9 (>2 km). These findings demonstrated the ability of the Doppler wind LiDAR system to monitor transboundary air pollution and provided a scientific reference for policy makers.

Financial support

This work was supported by the Natural Science Research of Jiangsu Higher Education Institutions of China [23KJB170012], and open fund of China Meteorological Administration Aerosol-Cloud and Precipitation Key Laboratory [KDW2403].

CRediT authorship contribution statement

Mengya Wang: Writing – original draft, Methodology, Investigation, Formal analysis. **Tianwen Wei:** Writing – review & editing, Methodology, Formal analysis, Conceptualization. **Simone Lolli:** Writing – review & editing, Visualization. **Kenan Wu:** Resources, Data curation. **Hainan Hu:** Visualization, Software. **Jinlong Yuan:** Resources, Data curation. **Dawei Tang:** Resources. **Haiyun Xia:** Validation, Supervision, Methodology, Conceptualization.

Declaration of competing interest

The contact author has declared that none of the authors has any competing interests.

Data availability

Measurement data from the field campaign used in this study are available from the corresponding author upon request (twwei@nuist.edu.cn).

Acknowledgements

We acknowledge the School of Earth and Space Science of USTC for providing the lidar observation. We acknowledge the High Performance Computing Center of Nanjing University of Information Science & Technology for their support of this work.We acknowledge the China National Environmental Monitoring Center (http://www.cnemc.cn/, last access: 25 March 2024), the ECMWF (https://cds.climate.copernicus.eu/cdsapp#!/dataset/reanalysis-era5-pressure-levels?tab=overview, last access: 25 March 2024), the NOAA (http://www.ftp.ncep.noaa.gov/data/nccf/com/gfs/prod/, last access: 25 March 2024), and the NASA (https://worldview.earthdata.nasa.gov/, last access: 25 March 2024) for providing air quality data, global reanalysis data, meteorological data, and aerosol depth data, respectively.

Appendix A. Supplementary data

Supplementary data to this article can be found online at https://doi.org/10.1016/j.atmosres.2024.107616.

References

Banah, V.A., Smalikho, I., 2013. Coherent Doppler Wind Lidars in a Turbulent Atmosphere. Artech House, London.

Banakh, V.A., Brewer, A., Pichugina, E.L., Smalikho, I.N., 2010. Measurements of wind velocity and direction with coherent Doppler lidar in conditions of a weak echo signal. Atmospher. Ocean. Opt. 23, 381–388. https://doi.org/10.1134/S1024856010050076.

Banakh, V.A., Smalikho, I.N., Falits, A.V., 2017. Estimation of the turbulence energy dissipation rate in the atmospheric boundary layer from measurements of the radial wind velocity by micropulse coherent Doppler lidar. Opt. Express 25, 22679. https://doi.org/10.1364/oe.25.022679.

Banakh, V.A., Smalikho, I.N., Falits, A.V., 2021. Estimation of the height of the turbulent mixing layer from data of doppler lidar measurements using conical scanning by a probe beam. Atmosph. Meas. Tech. 14, 1511–1524. https://doi.org/10.5194/amt-14-1511-2021.

Chi, X., Ma, X., Jiang, Q., You, Y., Guan, L., 2021. Analysis of the december 2020 atmospheric circulation and weather (in chinese). Meteorol. Monogr. 47, 381–388.

Chouza, F., Reitebuch, O., Groß, S., Rahm, S., Freudenthaler, V., Toledano, C., Weinzierl, B., 2015. Retrieval of aerosol backscatter and extinction from airborne coherent doppler wind lidar measurements. Atmosph. Meas. Tech. 8, 2909–2926. https://doi.org/10.5194/amt-8-2909-2015.

Cory-Slechta, D.A., Sobolewski, M., 2023. Neurotoxic effects of air pollution: an urgent public health concern. Nat. Rev. Neurosci. 24, 129–130. https://doi.org/10.1038/s41583-022-00672-8.

Draxler, R.R., Hess, G., 1998. An overview of the HYSPLIT_4 modelling system for trajectories, dispersion, and deposition. Aust. Meteorol. Mag. 47, 295–308.

Dupont, J.C., Haeffelin, M., Badosa, J., Elias, T., Favez, O., Petit, J.E., Meleux, F., Sciare, J., Crenn, V., Bonne, J.L., 2016. Role of the boundary layer dynamics effects on an extreme air pollution event in Paris. Atmos. Environ. 141, 571–579. https://doi.org/10.1016/j.atmosenv.2016.06.061.

Fang, Z., Yang, H., Cao, Y., Xing, K., Liu, D., Zhao, M., Xie, C., 2021. Study of persistent pollution in Hefei during winter revealed by ground-based LiDAR and the CALIPSO satellite. Sustain. Switz. 13, 1–15. https://doi.org/10.3390/su13020875.

Frehlich, R., 1996. Simulation of Coherent Doppler Lidar Performance in the Weak-Signal Regime. J. Atmos. Ocean. Technol. 13, 646–658. https://doi.org/10.1175/1520-0426(1996)013<0646:SOCDLP>2.0.CO;2.

Gu, Y., Yim, S.H.L., 2016. The air quality and health impacts of domestic trans-boundary pollution in various regions of China. Environ. Int. 97, 117–124. https://doi.org/10.1016/j.envint.2016.08.004.

He, Y., Li, L., Wang, H., Xu, X., Li, Y., Fan, S., 2022. A cold front induced co-occurrence of O3 and PM2.5 pollution in a Pearl River Delta city: Temporal variation, vertical structure, and mechanism. Environ. Pollut. 306, 119464 https://doi.org/10.1016/j.envpol.2022.119464.

Hirsikko, A., O'Connor, E.J., Komppula, M., Korhonen, K., Pfüller, A., Giannakaki, E., Wood, C.R., Bauer-Pfundstein, M., Poikonen, A., Karppinen, T., Lonka, H., Kurri, M., Heinonen, J., Moisseev, D., Asmi, E., Aaltonen, V., Nordbo, A., Rodriguez, E., Lihavainen, H., Laaksonen, A., Lehtinen, K.E.J.J., Laurila, T., Petäjä, T., Kulmala, M., Viisanen, Y., 2014. Observing wind, aerosol particles, clouds and precipitation: Finland's new ground-based remote-sensing network. Atmosph. Meas. Tech. 7, 1351–1375. https://doi.org/10.5194/amt-7-1351-2014.

Hong, Q., Liu, C., Hu, Q., Xing, C., Tan, W., Liu, H., Huang, Y., Zhu, Y., Zhang, J., Geng, T., Liu, J., 2019. Evolution of the vertical structure of air pollutants during winter heavy pollution episodes: the role of regional transport and potential sources. Atmos. Res. 228, 206–222. https://doi.org/10.1016/j.atmosres.2019.05.016.

Hu, Y., Dong, Q., 2021. Analysis of the february 2021 atmospheric circulation and weather (in Chinese). Meteorol. Monogr. 47, 638–644.

Hua, S., Zhang, T., Zhang, C., 2021. Analysis of the may 2021 atmospheric circulation and weather (in chinese). Meteorol. Monogr. 47, 1021–1028.

Huang, J., Pan, X., Guo, X., Li, G., 2018. Health impact of China's Air Pollution Prevention and Control Action Plan: an analysis of national air quality monitoring and mortality data. Lancet Planet. Health 2, e313–e323. https://doi.org/10.1016/S2542-5196(18)30141-4.

Huang, K., Ding, K., Yang, X.-J., Hu, C.-Y., Jiang, W., Hua, X.-G., Liu, J., Cao, J.-Y., Zhang, T., Kan, X.-H., Zhang, X.-J., 2020. Association between short-term exposure to ambient air pollutants and the risk of tuberculosis outpatient visits: a time-series study in Hefei, China. Environ. Res. 184, 109343 https://doi.org/10.1016/j.envres.2020.109343.

Huang, T., Yang, Y., O'Connor, E.J., Lolli, S., Haywood, J., Osborne, M., Cheng, J.C.H., Guo, J., Yim, S.H.L., 2021. Influence of a weak typhoon on the vertical distribution of air pollution in Hong Kong: a perspective from a Doppler LiDAR network. Environ. Pollut. 276, 116534 https://doi.org/10.1016/j.envpol.2021.116534.

Hung, W.-T., Lu, C.-H. Sarah, Alessandrini, S., Kumar, R., Lin, C.-A., 2020. Estimation of PM2.5 concentrations in New York state: understanding the influence of vertical mixing on surface PM2.5 using machine learning. Atmosphere 11, 1303. https://doi.org/10.3390/atmos11121303.

Jia, M., Yuan, J., Wang, C., Xia, H., Wu, Y., Zhao, L., Wei, T., Wu, J., Wang, L., Gu, S.Y., Liu, L., Lu, D., Chen, R., Xue, X., Dou, X., 2019. Long-lived high-frequency gravity waves in the atmospheric boundary layer: Observations and simulations. Atmos. Chem. Phys. 19, 15431–15446. https://doi.org/10.5194/acp-19-15431-2019.

Li, Z., Guo, J., Ding, A., Liao, H., Liu, J., Sun, Y., Wang, T., Xue, H., Zhang, H., Zhu, B., 2017. Aerosol and boundary-layer interactions and impact on air quality. Natl. Sci. Rev. 4, 810–833. https://doi.org/10.1093/nsr/nwx117.

Liu, C., Xing, C., Hu, Q., Li, Q., Liu, Haoran, Hong, Q., Tan, W., Ji, X., Lin, H., Lu, C., Lin, J., Liu, Hanyang, Wei, S., Chen, J., Yang, K., Wang, S., Liu, T., Chen, Y., 2022a. Ground-based hyperspectral stereoscopic remote sensing network: a promising strategy to learn coordinated control of O3 and PM2.5 over China. Engineering 19, 71–83. https://doi.org/10.1016/j.eng.2021.02.019.

Liu, H., Yue, F., Xie, Z., 2022b. Quantify the role of anthropogenic emission and meteorology on air pollution using machine learning approach: a case study of PM2.5 during the COVID-19 outbreak in Hubei Province, China. Environ. Pollut. 300, 118932 https://doi.org/10.1016/j.envpol.2022.118932.

Lolli, S., Sicard, M., Amato, F., Comeron, A., Gíl-Diaz, C., Landi, T.C., Munoz-Porcar, C., Oliveira, D., Dios Otin, F., Rocadenbosch, F., Rodriguez-Gomez, A., Alastuey, A., Querol, X., Reche, C., 2023. Climatological assessment of the vertically resolved optical and microphysical aerosol properties by lidar measurements, sun photometer, and in situ observations over 17 years at universitat politècnica de catalunya (UPC) Barcelona. Atmos. Chem. Phys. 23, 12887–12906. https://doi.org/10.5194/acp-23-12887-2023.

Luo, M., Hou, X., Gu, Y., Lau, N.-C., Yim, S.H.-L., 2018. Trans-boundary air pollution in a city under various atmospheric conditions. Sci. Total Environ. 618, 132–141. https://doi.org/10.1016/j.scitotenv.2017.11.001.

Mai, Z., Zhang, T., 2022. Analysis of the march 2022 atmospheric circulation and weather (in Chinese). Meteorol. Monogr. 48, 794–800.

Mai, Z., Zhang, T., Sheng, J., 2021. Analysis of the april 2021 atmospheric circulation and weather (in Chinese). Meteorol. Monogr. 47, 893–900.

Mao, M., Zhang, X., Shao, Y., Yin, Y., 2019. Spatiotemporal variations and factors of air quality in urban Central China during 2013–2015. Int. J. Environ. Res. Public Health 17, 229. https://doi.org/10.3390/ijerph17010229.

Mao, M., Rao, L., Jiang, H., He, S., Zhang, X., 2022. Air pollutants in metropolises of eastern coastal China. Int. J. Environ. Res. Public Health 19, 15332. https://doi.org/10.3390/ijerph192215332.

Miao, Y., Guo, J., Liu, S., Liu, H., Li, Z., Zhang, W., Zhai, P., 2017. Classification of summertime synoptic patterns in Beijing and their associations with boundary layer structure affecting aerosol pollution. Atmos. Chem. Phys. 17, 3097–3110. https://doi.org/10.5194/acp-17-3097-2017.

Miao, Y., Zhang, G., Li, X., Xue, C., 2023. Editorial: Physical and chemical processes within the planetary boundary layer and their impacts on air pollution. Front. Environ. Sci. 11, 1221546. https://doi.org/10.3389/fenvs.2023.1221546.

Nan, Y., Rao, X., You, Y., Guan, L., 2022. Analysis of the january 2022 atmospheric circulation and weather (in chinese). Meteorol. Monogr. 48, 526–532.

Nie, G., Gao, S., 2021. Analysis of the october 2020 atmospheric circulation and weather (in Chinese). Meteorol. Monogr. 47, 127–132.

O'Connor, E.J., Illingworth, A.J., Hogan, R.J., 2004. A technique for autocalibration of cloud lidar. J. Atmos. Ocean. Technol. 21, 777–786. https://doi.org/10.1175/1520-0426(2004)021<0777:ATFAOC>2.0.CO;2.

Ojha, N., Soni, M., Kumar, M., Gunthe, S.S., Chen, Y., Ansari, T.U., 2022. Mechanisms and Pathways for Coordinated Control of Fine Particulate Matter and ozone. Curr. Pollut. Rep. 8, 594–604. https://doi.org/10.1007/s40726-022-00229-4.

Pentikäinen, P., James O'connor, E., Juhani Manninen, A., Ortiz-Amezcua, P., 2020. Methodology for deriving the telescope focus function and its uncertainty for a heterodyne pulsed Doppler lidar. Atmosph. Meas. Tech. 13, 2849–2863. https://doi.org/10.5194/amt-13-2849-2020.

Qin, K., Wu, L., Wong, M.S., Letu, H., Hu, M., Lang, H., Sheng, S., Teng, J., Xiao, X., Yuan, L., 2016. Trans-boundary aerosol transport during a winter haze episode in China revealed by ground-based lidar and CALIPSO satellite. Atmos. Environ. 141, 20–29. https://doi.org/10.1016/j.atmosenv.2016.06.042.

Qu, Y., Wang, T., Wu, H., Shu, L., Li, M., Chen, P., Zhao, M., Li, S., Xie, M., Zhuang, B., Liu, J., Han, Y., 2020. Vertical structure and interaction of ozone and fine particulate matter in spring at Nanjing, China: the role of aerosol's radiation feedback. Atmos. Environ. 222, 117162 https://doi.org/10.1016/j.atmosenv.2019.117162.

Ren, B., Xie, P., Xu, J., Li, A., Qin, M., Hu, R., Zhang, T., Fan, G., Tian, X., Zhu, W., Hu, Z., Huang, Y., Li, X., Meng, F., Zhang, G., Tong, J., Ren, H., Zheng, J., Zhang, Z., Lv, Y., 2022. Vertical characteristics of NO2 and HCHO, and the ozone formation regimes in Hefei, China. Sci. Total Environ. 823, 153425 https://doi.org/10.1016/j.scitotenv.2022.153425.

Shen, L., Cheng, Y., Bai, X., Dai, H., Wei, X., Sun, L., Yang, Y., Zhang, J., Feng, Y., Li, Y.J., Chen, D.-R., Liu, J., Gui, H., 2022. Vertical profile of aerosol number size distribution during a haze pollution episode in Hefei, China. Sci. Total Environ. 814, 152693 https://doi.org/10.1016/j.scitotenv.2021.152693.

Shi, C., Yuan, R., Wu, B., Meng, Y., Zhang, Hao, Zhang, Hongqun, Gong, Z., 2018. Meteorological conditions conducive to PM2.5 pollution in winter 2016/2017 in the western yangtze river delta, China. Sci. Total Environ. 642, 1221–1232. https://doi.org/10.1016/j.scitotenv.2018.06.137.

Smalikho, I., 2003. Techniques of wind vector estimation from data measured with a scanning coherent Doppler Lidar. J. Atmos. Ocean. Technol. 20, 276–291. https://doi.org/10.1175/1520-0426(2003)020<0276:TOWVEF>2.0.CO;2.

Sulaymon, I.D., Zhang, Yuanxun, Hu, J., Hopke, P.K., Zhang, Yang, Zhao, B., Xing, J., Li, L., Mei, X., 2021. Evaluation of regional transport of PM2.5 during severe atmospheric pollution episodes in the western yangtze river delta, China. J. Environ. Manag. 293, 112827 https://doi.org/10.1016/j.jenvman.2021.112827.

Wang, M., Cao, C., Li, G., Singh, R.P., 2015. Analysis of a severe prolonged regional haze episode in the Yangtze River Delta, China. Atmos. Environ. 102, 112–121. https://doi.org/10.1016/j.atmosenv.2014.11.038.

Wang, H., Gao, S., Cao, Y., 2020. Analysis of the october 2019 atmospheric circulation and weather (in Chinese). Meteorol. Monogr. 46, 138–144.

Wang, L., Qiang, W., Xia, H., Wei, T., Yuan, J., Jiang, P., 2021. Robust solution for Boundary Layer Height Detections with Coherent Doppler Wind Lidar. Adv. Atmos. Sci. 38, 1920–1928. https://doi.org/10.1007/s00376-021-1068-0.

Wei, T., Xia, H., Hu, J., Wang, C., Shangguan, M., Wang, L., Jia, M., Dou, X., 2019. Simultaneous wind and rainfall detection by power spectrum analysis using a VAD scanning coherent Doppler lidar. Opt. Express 27, 31235. https://doi.org/10.1364/oe.27.031235.

Wei, T., Xia, H., Wu, Y., Yuan, J., Wang, C., Dou, X., 2020. Inversion probability enhancement of all-fiber CDWL by noise modeling and robust fitting. Opt. Express 28, 29662. https://doi.org/10.1364/oe.401054.

Wei, T., Xia, H., Yue, B., Wu, Y., Liu, Q., 2021. Remote sensing of raindrop size distribution using the coherent doppler lidar. Opt. Express 29, 17246. https://doi.org/10.1364/OE.426326.

Wei, T., Xia, H., Wu, K., Yang, Y., Liu, Q., Ding, W., 2022. Dark/bright band of a melting layer detected by coherent Doppler lidar and micro rain radar. Opt. Express 30, 3654. https://doi.org/10.1364/OE.450714.

Wiegner, M., Madonna, F., Binietoglou, I., Forkel, R., Gasteiger, J., Geiß, A., Pappalardo, G., Schäfer, K., Thomas, W., 2014. What is the benefit of ceilometers for aerosol remote sensing? An answer from EARLINET. Atmosph. Meas. Tech. 7, 1979–1997. https://doi.org/10.5194/amt-7-1979-2014.

Xia, Q., Zhang, X., Hu, Y., Tian, W., Miao, W., Wu, B., Lai, Y., Meng, J., Fan, Z., Zhang, C., Xin, L., Miao, J., Wu, Q., Jiao, M., Shan, L., Wang, N., Shi, B., Li, Y., 2022. The superposition effects of air pollution on government health expenditure in China—spatial evidence from GeoDetector. BMC Public Health 22, 1411. https://doi.org/10.1186/s12889-022-13702-y.

Xiang, Y., Zhang, T., Liu, J., Wan, X., Loewen, M., Chen, X., Kang, S., Fu, Y., Lv, L., Liu, W., Cong, Z., 2021. Vertical profile of aerosols in the himalayas revealed by lidar: New insights into their seasonal/diurnal patterns, sources, and transport. Environ. Pollut. Barking Essex 1987 (285), 117686. https://doi.org/10.1016/j.envpol.2021.117686.

Xing, J., Wang, J., Mathur, R., Wang, S., Sarwar, G., Pleim, J., Hogrefe, C., Zhang, Y., Jiang, J., Wong, D.C., Hao, J., 2017. Impacts of aerosol direct effects on tropospheric ozone through changes in atmospheric dynamics and photolysis rates. Atmos. Chem. Phys. 17, 9869–9883. https://doi.org/10.5194/acp-17-9869-2017.

Xu, R., Jiang, Q., Gui, H., You, Y., Guan, L., 2021. Analysis of the january 2021 atmospheric circulation and weather (in Chinese). Meteorol. Monogr. 47, 510–516.

Yan, Y., Cai, X., Miao, Y., Yu, M., 2022. Synoptic condition and boundary layer structure regulate PM2.5 pollution in the huaihe river basin, China. Atmos. Res. 269, 106041 https://doi.org/10.1016/j.atmosres.2022.106041.

Yang, Y., Yim, S.H.L., Haywood, J., Osborne, M., Chan, J.C.S., Zeng, Z., Cheng, J.C.H., 2019. Characteristics of Heavy Particulate Matter Pollution events over Hong Kong and their Relationships with Vertical Wind Profiles using High-Time-Resolution Doppler Lidar Measurements. J. Geophys. Res.-Atmos. 124, 9609–9623. https://doi.org/10.1029/2019JD031140.

Yang, S., Preißler, J., Wiegner, M., von Löwis, S., Petersen, G.N., Parks, M.M., Finger, D. C., 2020a. Monitoring dust events using doppler lidar and ceilometer in Iceland. Atmosphere 11, 1–23. https://doi.org/10.3390/atmos11121294.

Yang, Y., Zheng, Z., Yim, S.Y.L., Roth, M., Ren, G., Gao, Z., Wang, T., Li, Q., Shi, C., Ning, G., Li, Y., 2020b. PM2.5 Pollution Modulates Wintertime Urban Heat Island Intensity in the Beijing-Tianjin-Hebei Megalopolis, China. Geophys. Res. Lett. 47, 1–12. https://doi.org/10.1029/2019GL084288.

Yang, G., Ren, G., Zhang, P., Xue, X., Tysa, S.K., Jia, W., Qin, Y., Zheng, X., Zhang, S., 2021. PM 2.5 Influence on Urban Heat Island (UHI) effect in Beijing and the possible Mechanisms. J. Geophys. Res.-Atmos. 126 https://doi.org/10.1029/2021JD035227 e2021JD035227.

Ye, N., Kita, M., Matsubara, S., Okyere, S.A., Shimoda, M., 2021. Socio-spatial changes in danwei neighbourhoods: a case study of the AMS danwei compound in Hefei, China. Urban Sci. 5, 35. https://doi.org/10.3390/urbansci5020035.

Yim, S.H.L., Huang, T., 2023. Analysis of the air quality in upper atmospheric boundary layer in a high-density city in Asia using 3-year vertical profiles measured by the 3-Dimensional Real-Time Atmospheric monitoring System (3DREAMS). Sci. Total Environ. 857, 159137 https://doi.org/10.1016/j.scitotenv.2022.159137.

Zhang, Y., Guo, J., Yang, Y., Wang, Y., Yim, S.H.L., 2020a. Vertical wind shear modulates particulate matter pollutions: a perspective from radarwind profiler observations in Beijing, China. Remote Sens. 12 https://doi.org/10.3390/rs12030546.

Zhang, T., Xu, R., Gui, H., 2020b. Analysis of the november 2019 atmospheric circulation and weather (in chinese). Meteorol. Monogr. 46, 283–288.

Zhang, S., Zhou, Z., Ye, C., Shi, J., Wang, P., Liu, D., 2020c. Analysis of a Pollution Transmission Process in Hefei City based on Mobile Lidar. EPJ Web Conf. 237, 02006. https://doi.org/10.1051/epjconf/202023702006.

Zhao, X., Huang, K., Fu, J.S., Abdullaev, S.F., 2022. Long-range transport of asian dust to the arctic: Identification of transport pathways, evolution of aerosol optical properties, and impact assessment on surface albedo changes. Atmos. Chem. Phys. 22, 10389–10407. https://doi.org/10.5194/acp-22-10389-2022.

Zhao, S., He, J., Dong, L., Qi, S., Yin, D., Chen, J., Yu, Y., 2023. Contrasting vertical circulation between severe and light air pollution inside a deep basin: results from the collaborative experiment of 3D boundary-layer meteorology and pollution at the Sichuan basin (BLMP-SCB). Bull. Am. Meteorol. Soc. 104, E411–E434. https://doi.org/10.1175/BAMS-D-22-0150.1.

Zhou, J., 2002. Lidar observations of Asian dust over Hefei, China, in spring 2000. J. Geophys. Res. 107, 4252. https://doi.org/10.1029/2001JD000802.

Zhou, X., Zhang, T., 2020. Analysis of the march 2020 atmospheric circulation and weather (in chinese). Meteorol. Monogr. 46, 863–872.

Zong, L., Yang, Y., Gao, M., Wang, H., Wang, P., Zhang, H., Wang, L., Ning, G., Liu, C., Li, Y., Gao, Z., 2021. Large-scale synoptic drivers of co-occurring summertime ozone and PM2.5 pollution in eastern China. Atmos. Chem. Phys. 21, 9105–9124. https://doi.org/10.5194/acp-21-9105-2021.